JGR Earth Surface

RESEARCH ARTICLE
10.1029/2020JF006053

Special Section:
Fire in the Earth System

Movement of Sediment Through a Burned Landscape: Sediment Volume Observations and Model Comparisons in the San Gabriel Mountains, California, USA

F. K. Rengers[1], Luke A. McGuire[2], Jason W. Kean[1], Dennis M. Staley[1], Mariana Dobre[3], Peter R. Robichaud[4], and Tyson Swetnam[2]

[1]U.S. Geological Survey, Geologic Hazards Science Center, Golden, CO, USA, [2]University of Arizona, Tucson, AZ, USA, [3]University of Idaho, Moscow, ID, USA, [4]Department of Agriculture, U.S. Forest Service, Rocky Mountain Research Station, Moscow, ID, USA

Key Points:

- The majority of sediment eroded after a wildfire in the San Gabriel Mountains originated from hillslopes
- Post-fire sediment volumes were best predicted by an empirical model developed in the same physiographic region
- Year one post-wildfire erosion rates are similar in magnitude to the long-term bedrock erosion rates in the San Gabriel Mountains

Supporting Information:

Supporting Information may be found in the online version of this article.

Correspondence to:

F. K. Rengers,
frengers@usgs.gov

Citation:

Rengers, F. K., McGuire, L. A., Kean, J. W., Staley, D. M., Dobre, M., Robichaud, P. R., & Swetnam, T. (2021). Movement of sediment through a burned landscape: Sediment volume observations and model comparisons in the San Gabriel Mountains, California, USA. *Journal of Geophysical Research: Earth Surface*, *126*, e2020JF006053. https://doi.org/10.1029/2020JF006053

Received 22 DEC 2020
Accepted 4 JUN 2021

Abstract Post-wildfire changes to hydrologic and geomorphic systems can lead to widespread sediment redistribution. Understanding how sediment moves through a watershed is crucial for assessing hazards, developing debris flow inundation models, engineering sediment retention solutions, and quantifying the role that disturbances play in landscape evolution. In this study, we used terrestrial and airborne lidar to measure sediment redistribution in the 2016 Fish Fire, in the San Gabriel Mountains in southern California, USA. The lidar areas are in two adjacent watersheds, at spatial scales of 900 m^2 to 4 km^2, respectively. Terrestrial lidar data were acquired prior to rainfall, and two subsequent surveys show erosional change after rainstorms. Two airborne lidar flights occurred (1) 7 months before, and (2) 14 months after the fire ignition, capturing the erosional effects after rainfall. We found hillslope erosion dominated the overall sediment budget in the first rainy season after wildfire. Only 7% of the total erosion came from the active channel bed and channel banks, and the remaining 93% of eroded sediment was derived from hillslopes. Within the channelized portion of the watershed erosion/deposition could be generally described with topographic metrics used in a stream power equation. Observed sediment volumes were compared with four empirical models and one process-based model. We found that the best predictions of sediment volume were obtained from an empirical model developed in the same physiographic region. Moreover, this study showed that post-wildfire erosion rates in the San Gabriel Mountains attain the same magnitude as millennial time scale bedrock erosion rates.

Plain Language Summary Debris flows are mixtures of water and sediment that move swiftly downhill, damaging property and threatening lives. Rainfall on steep mountainous slopes burned by wildfire can generate these debris flows, creating a substantial risk. It is difficult to create evacuation plans or to build appropriate mitigation structures to capture debris flow sediment downstream of steep, burned slopes if we don'|'t know how to estimate the volume of sediment that might flow downhill. This study uses observations of erosion and deposition in a burned watershed to calculate the volume of sediment moved, and to map where the sediment was removed and deposited. We compared the observations with known models to test the model predictions. We found that most of the sediment was moved from hillslope areas, and then redeposited downstream in low-lying areas of the channel, primarily downstream of the mountain front.

1. Introduction

Wildfire creates conditions that are favorable for water runoff and sediment transport. For example, infiltration is often reduced after wildfire due to enhanced water repellant conditions (DeBano, 2000; DeBano et al., 1979), hyper-dry conditions (Moody & Ebel, 2012), and/or surface soil sealing (Larsen et al., 2009). In addition, more rainfall can reach the forest floor when the canopy burns because of a loss of interception (Valente et al., 1997). Water runoff is increased by a lack of ground cover (e.g., vegetation, litter, and duff), resulting in reduced water storage (Larsen et al., 2009; Parise & Cannon, 2012) and lower roughness (Cerdà & Doerr, 2005; Liu et al., 2021; Noske et al., 2016). Additionally, wildfire can propagate high temperatures into the soil (Rengers et al., 2017) making soil more erodible (Moody et al., 2005) by killing fine roots (Busse et al., 2010; Chief et al., 2012; Hungerford et al., 1991; Nyman et al., 2013), destroying expansive

clay particles (Arocena & Opio, 2003; Chandler et al., 1983; Fitzpatrick, 1980; Ulery et al., 1996), and killing soil stabilizing bacteria and fungi (DeBano et al., 1979). Wildfire-induced changes to soils and vegetation thus collectively increase water runoff and sediment availability. Because these post-wildfire conditions are conducive to sediment transport, burned watersheds often produce substantially more erosion during rainfall than nearby unburned watersheds. Post-wildfire erosion has even been found to generate the majority of long-term erosion in some mountain systems (Kirchner et al., 2001; Ellett et al., 2019; Orem & Pelletier, 2015). Consequently, understanding how fire influences both short-term hazards, such as debris flows (Cannon, 2001; Cannon & DeGraff, 2009; Cannon et al., 2003; Kean et al., 2011, 2012; Nyman et al., 2011; Palucis et al., 2021), and longer-term geomorphic changes to the landscape (Meyer et al., 1992; Pierce & Meyer, 2008), requires datasets that quantify the spatial redistribution of sediment through hillslope-channel systems following fire.

The coupled hillslope and channel system in a watershed develops over geologic time, balanced by the tectonic and climatic forces of a region (e.g., Tucker et al., 2001), but the short-term effects of wildfire can alter the geomorphic processes that determine the sediment budget in that system. Conceptually, sediment moves through hillslopes and channels via sediment cascades (Fryirs, 2013). Sediment cascades represent the diversity of sediment delivery systems in a watershed (e.g., hillslope diffusion, landsliding, overland flow), where sediment moves from positions of high potential energy to low potential energy. Low sloping landforms such as hillslopes, colluvial hollows, channel bars, floodplains, and terraces can act as sediment reservoirs (Bennett et al., 2014) to store sediment, and on steep hillslopes vegetation stems/trunks can also serve to dam and store sediment (DiBiase & Lamb, 2013). The sediment cascade conceptual model creates a useful framework to explore and describe wildfire-induced changes. The sediment cascade is composed of geomorphic process domains (Wohl, 2010) that operate at different spatial scales [e.g., rainsplash (Gabet & Dunne, 2003; Moss, 1988; Moss et al., 1979) at 1×10^{-1} m to debris flows (Kean, Staley, et al., 2019; Prochaska, Santi, Higgins, & Cannon, 2008) at 1×10^{6} m] and temporal scales [e.g., nearly instantaneous dry-ravel during fire (DiBiase & Lamb, 2013) to landslides years to decades after wildfire (De Graff, 2018; Jackson & Roering, 2009; Rengers et al., 2020)].

Research over the past few decades has provided insight into the geomorphic processes that make up the sediment cascade after wildfire, and that work can be used to develop a general conceptual understanding of sediment movement in burned watersheds. At the hillslope scale, fire can burn temporary vegetation dams, creating gravitationally unstable conditions such that dry ravel moves sediment downhill, leading to aggradation on low angle slopes or in channels (DiBiase & Lamb, 2013, 2020; Florsheim et al., 1991, 2016; Gabet, 2003; Lamb et al., 2011). Rainfall on burned slopes contributes to a range of sediment transport processes on hillslopes facilitated by raindrop impact, sheetflow, and concentrated overland flow (e.g., rills; McGuire et al., 2016; DeLong et al., 2018). Rills are small channelized erosional features often <10 cm in depth that form through overland flow incision, but can be infilled through deposition and often do not reform in the same location (Bull & Kirkby, 1997; McGuire et al., 2013). Rills are more efficient at transporting sediment than sheetflow because the channelized flow that develops within a rill creates greater hydraulic power than that on an unchannelized hillslope (Meyer et al., 1975; Pietraszek, 2006). Prior studies have documented that a majority of sediment on hillslopes is eroded via dry ravel, rainsplash, rilling, and/or sheetflow erosion (DiBiase & Lamb, 2020; Rengers, Tucker, Moody, et al., 2016; Staley et al., 2014).

The transition from hillslopes to channels occurs at channel heads (Dietrich & Dunne, 1993). Following wildfire, channel heads can migrate upstream (Wohl, 2013; Wohl & Scott, 2017), as colluvial hollows become sites for gully rejuvenation (Hyde et al., 2007, 2014) scouring into defined channels (Guilinger et al., 2020; Rengers, Tucker, Moody, et al., 2016; Rengers et al., 2018). Gullies are incisional channels subject to ephemeral flow that migrate upstream through headcut erosion (Rengers & Tucker, 2015), but unlike rills they are not rapidly infilled and can persist on a landscape for decades or longer (Rengers, Lunacek, & Tucker, 2016; Rengers & Tucker, 2014; Rengers et al., 2016). This extended channel network increases connectivity between hillslopes and channels (e.g., Wester et al., 2014). Coarse sand and gravel moved from hillslopes into the channel network (Brogan et al., 2017, 2019) continue downstream via bedload transport in subsequent flows (Moody & Martin, 2001; Reneau et al., 2007). During high intensity rainfall, sediment concentrations can become sufficiently high to generate debris flows via progressive entrainment or en masse failure of channel bed sediment (McGuire et al., 2017) transporting high volumes of sediment through a channel

network (Cannon et al., 2010; DeLong et al., 2018; Gartner et al., 2014; Nyman et al., 2020; Pelletier & Orem, 2014; Santi et al., 2008). Here we define debris flows as water-sediment mixtures with sediment concentrations exceeding 50% by volume, that flow under the force of gravity (e.g., Iverson, 1997). Finally, the sediment moved during these flows can deposit downstream as alluvial fans (Benda, 1990; Benda & Dunne, 1997; Ellett et al., 2019; Jordan, 2016; Kean, Staley, et al., 2019; Meyer & Wells, 1997) or within a dendritic channelized network (Murphy et al., 2019; Nyman et al., 2020; Pelletier & Orem, 2014).

In this study, we explored the spatial patterns and controls on erosion and deposition at the watershed scale (4.2 km^2) using two airborne lidar datasets, one obtained before a wildfire and the second obtained after a series of debris flow and flood-producing rain events. These watershed scale observations were further augmented by repeat terrestrial lidar data at the hillslope scale (900 m^2) that were used to document centimeter-scale changes during rain events. Using this combination of airborne and terrestrial lidar data, we investigated how spatial patterns of erosion/deposition change at different scales in burn areas. From this dataset, we focused our study on two primary research questions. (1) What are the dominant erosion sources and deposition sinks that lead to the spatial reorganization of sediment throughout the landscape? (2) How does the observed volume of sedimentation compare to the volume predicted by existing models?

These two research questions allow us to focus on important knowledge gaps, that is, the geomorphic controls on the source-sink of post-wildfire sediment and the volume of that sediment redistribution. To address question 1, we explored the role of topography (i.e., slope and drainage area) in determining the source-sink patterns of sediment at the watershed scale. Using the combined lidar data, we constrained sediment yield as a function of drainage area within the study watershed. We also placed the observed post-wildfire erosion rates within a context relevant to landscape evolution using observations of long-term erosion rates in the San Gabriel Mountains. Question two offered an opportunity to test observations of spatially continuous, post-wildfire sediment redistribution against several post-wildfire erosion models. Specifically, we compared our observations with sediment volumes predicted from models developed from (i) post-wildfire debris flows observations in southern California (Gartner et al., 2014) and New Mexico (Pelletier & Orem, 2014), (ii) post-wildfire erosion observations from across the western U.S. (Wagenbrenner & Robichaud, 2014), (iii) a post-wildfire sediment budget study tracking sediment from debris flow-producing headwaters into a fluvially dominated river system in Australia (Nyman et al., 2020), and (iv) the widely used process-based WEPP model (e.g., Robichaud et al., 2019). A better understanding of the best approach for predicting post-wildfire sediment volumes is important to early warning systems (e.g., NOAA, 2005), although we recognize that the best post-wildfire volume equations may be regionally dependent and this study only evaluates one location in southern California.

2. Study Site

The study site is located in the front range of the San Gabriel Mountains, southern California, USA, near the San Gabriel River, and was burned by the 2016 Fish Fire (part of the San Gabriel Complex) that started on 20 June 2016 and was contained by 23 July 2016 (Figure 1). The study site has a Mediterranean climate, with the majority of precipitation occurring in the winter months, followed by dry summer months (Bull, 1991). The mean annual precipitation at the site ranges from 600 to 950 mm (PRISM Climate Group Oregon State University, 2004). The winter rainstorms in southern California that result in post-fire debris flows are often associated with atmospheric river-type storms (Oakley et al., 2017) or narrow cold frontal rain bands (Oakley et al., 2018).

This study site is predominantly composed of tonalite of San Gabriel Reservoir (Cretaceous age) and layered gneiss (Proterozoic age; Morton & Miller, 2003) and is uplifting rapidly, which produces steep slopes (Bull, 1991) with shallow soils (DiBiase et al., 2010). The soils at the study site are typically composed of gravelly sandy loams (U.S. Department of Agriculture, 2020), and the soil depth is typically <50 cm, based on observations at shallow landslide scarps (Rengers et al., 2020).

We established hydrologic monitoring stations in two watersheds within the burn area, Las Lomas (0.12 km^2) (Kean, Smith, et al., 2019; Tang et al., 2019) and Van Tassel (4.2 km^2) (Michel et al., 2019; Figure 1) that recorded a series of debris flows and floods in the time period between the two airborne lidar surveys. The watersheds were primarily composed of a chaparral ecosystem prior to the fire, which burned at moderate

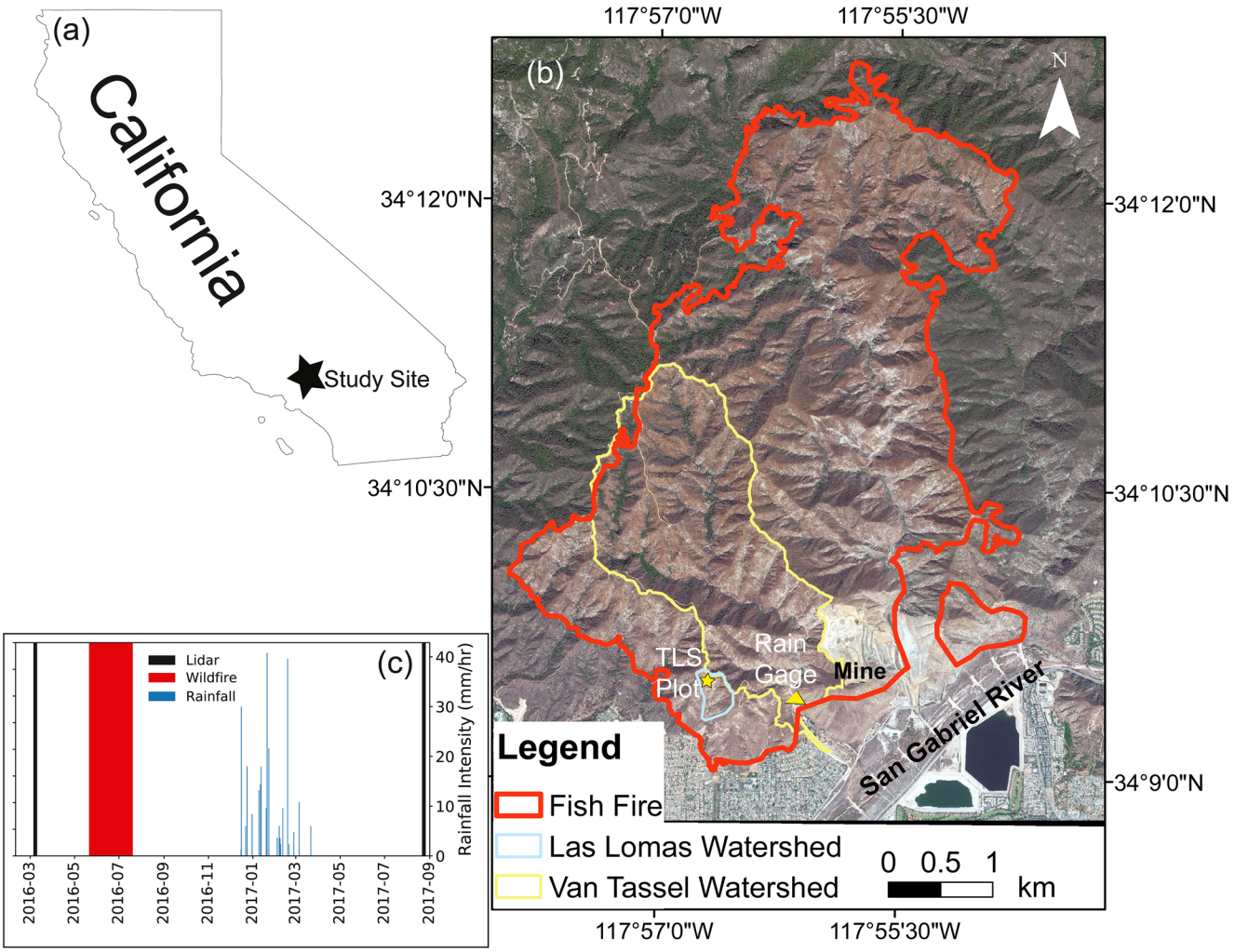

Figure 1. (a) Location of the study site within the state of California, USA. (b) Site map where star represents location of the terrestrial lidar plot and triangle represents the Van Tassel rain gage. The base map is Digital Globe imagery from September 18, 2018. (c) Timeline of lidar acquisition, wildfire duration, and rainfall intensity.

to high severity as defined by Parsons et al. (2010) throughout the majority of the study area (>80% of the Van Tassel watershed and >52% of the Las Lomas watershed). The Van Tassel watershed is used to explore erosion at a large watershed scale in this study, whereas more focused measurements of hillslope erosion are explored in the Las Lomas watershed in an area burned 100% at moderate to high severity. Analyzing these different locations as a nested analysis is comparable because these areas are similar in location, lithology, climate, tectonic history, and ecosystem, and were burned during the same fire.

3. Methods

3.1. Lidar Acquisition and Processing

We obtained repeat lidar datasets from both airborne and terrestrial platforms to show the evolution of erosion and deposition of the burned area at different scales. Airborne lidar was flown over the study area by Los Angeles County prior to the fire between December 20, 2015 and March 8, 2016. A second flight was commissioned by the U.S. Geological Survey (USGS) after the fire, and it was flown between August 11 and 24, 2017. The airborne lidar point clouds were both referenced to the horizontal datum NAD83 UTM Zone 11N, and NAVD88 was used as the vertical datum. The average point density of the ground-return points for the airborne lidar surveys is 2.8 pts/m^2.

We estimated erosion and deposition in the Van Tassel watershed from the vertical elevation change in the airborne lidar point clouds (e.g., Bernard et al., 2020). This point cloud change difference was estimated using the vertical option with the M3C2 software (Lague et al., 2013). M3C2 requires a projection scale (d) to establish the diameter of a moving cylinder. Using the guidance in Lague et al. (2013), we chose $d = 3$ m because a cylinder of that diameter would capture at least five points for 95% of the point cloud area in both point clouds. In addition, M3C2 also requires a normal scale D that defines the size of a spherical neighborhood around each core point, and Lague et al. (2013) found that D can be estimated using:

$$\frac{D}{\sigma(d)} > 25 \tag{1}$$

where $\sigma(d)$ represents the slope-normalized standard deviation of elevation, which serves as a proxy for roughness. We found that $D = 2$ m best enforces the ratio for both point clouds over 96% of the point cloud. Finally, a maximum depth is required for M3C2, and here we used 10 m. We subsequently gridded the vertical change point data to a raster with 0.5×0.5 m pixel spacing, and we estimated volumes by multiplying the pixel area by the vertical change in each pixel.

In order to estimate lidar data uncertainty, we compared before/after digital elevation models (DEMs) at transects along stable features (roads) following the methods of DeLong et al. (2012). We extracted four transects perpendicular to different roads, using two paved roads (outside of the Van Tassel watershed) and two dirt roads (located within the Van Tassel watershed) as stable features for comparison. The dirt road transects have greater topographic relief and highlight errors in registration based on terrain slope effects better than the paved roads alone. The maximum change in the stable features was considered as our registration error. In addition, we estimated the point cloud uncertainty level of detection (LoD) based on roughness and point density at a 95% confidence interval ($LoD_{95}(d)$) using James et al. (2017):

$$LoD_{95}(d) = \pm 1.96\left(\sqrt{\frac{\sigma_1(d)^2}{n_1} + \frac{\sigma_2(d)^2}{n_2}}\right) \tag{2}$$

where $\sigma_1(d)$ and $\sigma_2(d)$ are the roughness of the two different point clouds and n_1 and n_2 are the number of points in the two different point clouds. Finally, we excluded change data in areas that were steeper than 45° because in this mountain range those areas are largely bedrock outcrops (DiBiase et al., 2012).

A series of three terrestrial laser scanner (TLS) surveys were conducted on a 900 m^2 hillslope portion of the Las Lomas watershed using a Leica ScanStation C10 within a four-month period (Figure 1 shown as a star; McGuire & Rengers, 2019; Rengers & McGuire, 2018; Tang et al., 2019). The first TLS survey was conducted on November 19, 2016 after the wildfire and prior to any rainfall. The second TLS survey on January 5, 2017 was obtained following several rain events. On February 22, 2017, a third TLS survey took place following several more rain events and after the regrowth of some vegetation. Vegetation was removed from the point cloud using the CANUPO software (Brodu and Lague, 2012). The average point density of the ground-return points for the terrestrial lidar data is 5,200 pts/m^2. The TLS data were registered to a local coordinate system using a series of permanent control points (McGuire & Rengers, 2019; Tang et al., 2019). Topographic change between the surveys was estimated in the TLS survey area with the vertical M3C2 point cloud differencing approach (Bernard et al., 2020; Lague et al., 2013), similar to the airborne lidar data. Using the same procedure as with the airborne lidar data we chose $d = 0.06$ m, $D = 0.6$ m, and the maximum depth was set to 3 m. The vertical change point data were gridded to 0.025×0.025 m pixel spacing, and volumes were estimated by multiplying the pixel area by the vertical change in each pixel.

We used the TLS lidar data to quantify the amount of rill and interrill erosion with a multi-step approach to define rills. A Gaussian filter was used on the lidar DEM to smooth the topography, and this smoothed DEM was then differenced with the original topography to identify depressions (Rengers & McGuire, 2018). This effectively identified the rill areas; however, it also included some areas that were merely depressions where there was no surface change. We then selected the depressions that had sustained more erosion than the LoD to ensure that we were identifying areas of topographic change. This was followed with manual editing to remove any non-rill areas, which differs from the approach used in (Rengers & McGuire, 2018). Interrill areas were subsequently defined as any non-rill areas of elevation change > the LoD (Figure S1). In addi-

tion, we visually observed dry ravel fans in the first TLS survey. We estimated the volume of these fans by clipping the points around the fans from the first survey. In order to estimate the depth of the fan, we used the lidar from the third survey that captured rills cutting through the fans, and we used the minimum elevation points in the rilled areas of the fans to interpolate a pre-fan topographic surface. We then estimated the total volume of the fans by differencing the fan surface from the interpolated pre-fan topography. This approach assumes that the rills more easily eroded the dry ravel in the fans and the rill bottom was near the top of the pre-fan topography.

3.2. Sediment Budget

We used the vertical M3C2 airborne lidar difference to examine the sediment budget in the Van Tassel watershed. Our sediment budget divided the landscape into different landform categories according to the upstream contributing drainage area. Hillslopes represent all areas <1,000 m^2, small tributary channels are represented by areas from 1,000 to 10,000 m^2, larger axial channels are represented by areas from 10,000 to 3,000,000 m^2, and the primary axial channel near the mountain front is represented by areas >3,000,000 m^2. This sediment budget represents the volume change in the sources and sinks of sediment movement between the lidar flights. We focus on volume change using the vertical M3C2 elevation difference rather than mass change because our underlying dataset is best suited to detect volume differences, and we do not have widespread data on variations in sediment density that would lead to a reliable conversion from volume to mass. However, the TLS data revealed that substantial erosion is possible on the hillslopes below the airborne lidar level of detection. Consequently, we multiplied the TLS hillslope erosion (m) by the area within the Van Tassel watershed (m^2) that was (1) < the airborne lidar LoD, and (2) had a slope <45° to estimate a potential volume of sediment eroded below the airborne lidar LoD, using the assumption that slopes >45° are largely bedrock outcrops (DiBiase et al., 2012). The average slope of the TLS survey plot (39°) is similar to the average slope in the airborne lidar area <the LoD and <45° (36°), making this a reasonable comparison.

To examine the sediment budget within the confined canyon of the Van Tassel watershed (before exiting the mountain front where the channel becomes primarily depositional), we used a height above nearest drainage (HAND) analysis (Nobre et al., 2011). HAND is used to calculate the height of each pixel in a DEM above the nearest drainage, where drainage lines (i.e., the channel thalweg) are estimated using a D8 flow accumulation algorithm (Tarboton et al., 1991). We defined channel initiation using an upstream flow accumulation area of 1,000 m^2 based on slope-area observations suggesting that 1,000 m^2 is near the onset of fluvial channels in the San Gabriel Mountains (Rengers et al., 2019). This low drainage area estimate is conservative and may include some areas that were convergent but unchannelized prior to wildfire erosion. We explored the total erosion/deposition change (i.e., net erosion) in three distinct HAND elevation zones: (1) <0.5 m above the pre-fire DEM channel thalweg, which we consider the active channel (zone 1); (2) 0.5–3 m above the pre-fire DEM channel thalweg, which we consider the channel banks (zone 2); and (3) >3 m above the pre-fire DEM channel thalweg, which we consider the hillslopes (zone 3). These pre-defined zones were based on field observations and used in lieu of manual landform mapping in order to allow for objectivity and repeatability. This HAND analysis helps to describe the magnitude and sources of the net erosion within a narrow channel corridor. In particular, it can help to determine if sediment entrained by post-wildfire flows originates primarily from the active channel bed (Gregoretti & Fontana, 2008; Takahashi, 1978), the channel banks (Hungr et al., 2005), or from hillslopes (McGuire et al., 2016, 2017; Tillery & Rengers, 2020).

3.3. In-Channel Sedimentation Controls

We sought a general approach to explore controls on erosion and deposition within the channel network. Prior work has shown that stream power (ω) (Fuller, 2008; Surian et al., 2016; Thompson & Croke, 2013; Yochum et al., 2017), a stream power index (Nyman et al., 2015), or gradients in stream power (Gartner et al., 2015) can be used to estimate whether a channel reach will be dominantly erosional or depositional. Here ω (W/m^2) is defined as:

$$\omega = \frac{\rho g Q S_f}{B} \tag{3}$$

where ρ is the density of water (kg/m^3), g is gravitational acceleration (m^2/s), Q is the discharge (m^3/s), S_f is the channel friction slope (m/m), and B is the channel width (m). We can redefine the discharge in Equation 3 (e.g., Tucker & Bras, 2000) to obtain:

$$\omega = \rho g (P - I) \alpha \tag{4}$$

and

$$\alpha = \frac{A S_f}{B} \tag{5}$$

where P is the precipitation rate (m/s), I is the infiltration rate (m/s), A is the drainage area (m^2), α is a topographic factor (m) that can be estimated from a DEM for any cross section within a channel. In real-world prediction scenarios, information about potential erosion/deposition is needed before any rainfall is measured, therefore we focus solely on the topographic drivers that control stream power, that is, Equation 5. The topographic drivers of stream power are explored in order to determine if the geomorphology alone can provide a proxy for estimating zones of erosion or deposition without the need for estimates of precipitation or infiltration. We measured the channel width from the airborne lidar DEM at 50 m intervals along the longest drainage in the Van Tassel watershed, using the abrupt break in slope between the valley walls and the channel bed to define the active channel width. In order to determine α, the maximum drainage area was used at each channel width measurement and the slope (S_f) was calculated as the change in elevation divided by the length between channel width measurements (50 m). By comparing α with the net elevation change at each width transect, we explored how the topographic controls on stream power influenced whether a local stream reach was erosional or depositional. Unlike a full stream power analysis that would rely on estimating the flow discharge, this comparison using α only requires topographic metrics. Moreover, we performed this analysis in the portion of the channel upstream of the mountain front in the same area as the HAND analysis because the abrupt change in slope at the mountain front likely induces a rapid dewatering of the material, creating a less consistent comparison of the stream power estimate. Finally, if a stream power approach represents a hypothesis that flow mechanics dictated by topography govern channel erosion and deposition, an alternative hypothesis would be that tributary inputs of sediment overwhelm the flow mechanics. Therefore, as a contrast to the stream power exploration, we also explored the importance of elevation change at the channel cross sections with respect to distance downstream from the nearest tributary with a drainage area $>1 \times 10^5$ m^2.

3.4. Sediment Yield

In addition to exploring the sediment budget, we also sought to understand how sediment yields varied spatially throughout the burned watershed. Here, we used a method described in Pelletier and Orem (2014) to determine how sediment was routed through the study watershed in order to determine a sediment yield for each pixel in the DEM. In this approach, we first employ a multiple flow direction (MFD) flow-routing algorithm to calculate how mass (e.g., water, sediment, etc.) would be partitioned from one pixel to downstream pixels. Then starting from the most upstream pixel, the volume change (either erosion or deposition) is added to the change in the downstream pixels following the MFD defined route, and the change volume is cumulatively summed throughout the watershed to the pixel with the lowest elevation. In this way, it is possible to show the total volume of sediment that passes through different portions of the watershed. Finally, the sediment yield (m^3/m^2) is estimated by dividing the total volume of sediment passing through a given pixel by the contributing drainage area for that pixel.

Subsequently, we examined how the sediment yield varied across the landscape to investigate possible controlling factors. For a complete watershed scale analysis, we created a slope-area plot, using evenly spaced logarithmic bins for drainage areas between 10 m^2 and 4×10^6 m^2, and within each drainage area bin, we found the corresponding median slope, total sediment yield, and total sediment volume.

Table 1
Rainfall Van Tassel Rain Gage

Time peak intensity (dd-mm-yyyy HH:MM:SS)	10-min intensity (mm/h)	15-min intensity (mm/h)	Total accumulation (mm)	Duration (min)
16-12-2016 04:56:00	30.0	28.0	60.0	1645
22-12-2016 02:04:00	6.0	4.8	20.4	1381
24-12-2016 01:43:00	18.0	15.2	39.4	428
31-12-2016 00:01:00	8.4	5.6	23.4	2160
09-01-2017 05:35:00	13.2	12.0	21.4	476
11-01-2017 08:58:00	14.4	13.6	60.6	1391
12-01-2017 10:07:00	18.0	16.8	57.0	1133
19-01-2017 08:43:00	9.6	8.0	18.0	340
20-01-2017 13:48:00	40.8	33.6	63.0	1094
23-01-2017 00:28:00	21.6	20.0	94.0	2274
03-02-2017 11:04:00	3.6	4.0	3.6	329
06-02-2017 05:10:00	6.0	5.6	13.0	552
07-02-2017 09:08:00	3.6	2.4	5.0	509
08-02-2017 02:41:00	2.4	2.4	3.2	314
11-02-2017 05:05:00	9.6	8.8	15.0	1021
17-02-2017 18:54:00	39.6	36.8	69.4	816
19-02-2017 08:50:00	2.4	2.4	1.4	106
05-03-2017 15:51:00	10.8	7.2	6.2	148
21-03-2017 16:50:00	6.0	4.0	6.8	871

Note. Rain was considered part of the same storm if there was <8 h without 0.2 mm of additional rainfall.

3.5. Model Testing

Airborne lidar allowed us to generate spatially continuous estimates of erosion and deposition after the wildfire, which created an opportunity to test existing equations for predicting post-wildfire erosion volumes. We tested four published empirical models calibrated on wildfires in the western U.S., and one process-based model popular with land managers.

Our first test compared the observed net erosional volume within the Van Tassel watershed, with a prediction for post-wildfire sediment volume using the model proposed by Gartner et al. (2014):

$$ln(V) = 4.22 + 0.39\sqrt{i_{15}} + 0.36ln(Bmh) + 0.13\sqrt{R} \quad (6)$$

where V is volume (m^3), i_{15} is the 15-min rainfall intensity (mm/h) (Table 1), Bmh is watershed area burned at moderate and high severity (km^2), and R is the watershed relief (m). Equation 6 was developed based on 92 observations of post-wildfire debris flow volumes obtained from debris basins in the Transverse Ranges of southern California with watershed areas ranging from 0.01 to 27.9 km^2. Rather than applying Equation 6 to the entire Van Tassel watershed to obtain a single volume estimate, we instead broke the watershed into smaller sub-basins (from 0.02 to 4.2 km^2) using the Basin tool in ArcGIS 10.6 to compare predicted and observed volumes in multiple sub-basins (Figure S2). Since the erosion estimated from the lidar data encompass several rainstorms, for each sub-basin we calculated a volume per storm and then summed the volume from all the storms to get a total volume from Equation 6. The rainfall data were obtained from a rain gage located in the Van Tassel watershed (near triangle on Figure 1).

Using the same sub-basins, we tested a sediment yield model developed by Pelletier and Orem (2014) based on debris flow observations in the Jemez Mountains in New Mexico after the Las Conchas Fire:

$$Y_p = aS^bB_s^c \quad (7)$$

where Y_p is sediment yield (mm), S is average slope (m/m), B_s is the average soil burn severity class over the total sub-basin area (using low = 1, moderate = 2, high = 3), $a = 1.53$, $b = 1.6$, and $c = 1.7$. The sediment yield Y_p was subsequently converted from units of mm to m and multiplied by the watershed area in order to obtain a volume.

The third model we tested was developed by Wagenbrenner and Robichaud (2014) based on post-fire erosion studies in Colorado, Washington, Utah, Montana, and Arizona at scales <1.2 km^2:

$$Y_w = k_iA^{-0.21} \quad (8)$$

$$k_i = 10^{-0.018C_n + 0.042I_{10} + b_n} \quad (9)$$

where Y_w is sediment yield (Mg/ha), A is area (m^2), C_n is the average percent ground cover (%), I_{10} is 10-min precipitation intensity (mm/h), and b_n is 0.19. Here, percent ground cover was determined as a function of the burn severity using the burn severity to ground cover conversion used in WEPPcloud PeP (Robichaud et al., 2019), where no burn = 95% ground cover, low severity = 80% ground cover, moderate severity = 45% ground cover, and high severity = 30% ground cover. C_n was calculated as the average ground cover percentage across each sub-basin. The sediment yield estimated with Equations 8 and 9 was converted to a volume by multiplying Y_w by the sub-basin area and then dividing by a soil density. We did not have direct soil density measurements, so we used an average value from several burn areas in the western U.S. (1.14 Mg/m^3) (Robichaud et al., 2008).

The fourth model we tested was developed by Nyman et al. (2020):

$$V = eA^{0.73} \tag{10}$$

where $e = 0.35$ ($m^{1.37}$). Equation 10 is based on a combination of modeling and channel change measurements in a 14 km^2 burned watershed in Australia (Nyman et al., 2020).

Lastly, we tested the Water Erosion Prediction Project-Post-fire Erosion Prediction (WEPPcloud-PEP) model developed by the U.S. Forest Service and the University of Idaho (Robichaud et al., 2019). WEPPcloud-PEP is a process-based, post-wildfire erosion prediction model that runs the WEPP watershed model in a cloud environment, and is widely used by land managers to predict the effects of land management changes and wildfire on soil erosion and runoff (Ferná ndez & Vega, 2018; Gould et al., 2016). WEPP was originally developed for agricultural lands to simulate erosional processes including, rill and interrill erosion as well as concentrated flow (Flanagan & Livingston, 1995; Flanagan et al., 2001; Laflen et al., 1997). It has been adapted to simulate erosion in steeper forested and rangeland environments that have been burned by wildfire (Elliot et al., 1999). WEPPcloud-PEP generates daily weather data including: the total rainfall, storm duration, time-to-peak, peak intensity, minimum and maximum temperature, solar radiation, wind speed, and the dewpoint temperature via CLIGEN and PRISM (PRISM Climate Group Oregon State University, 2004; Robichaud et al., 2007). The WEPPcloud-PEP online interface offers several options for the users to build climate files based on observed precipitation and temperature data from national gridded datasets or stochastically generated weather files from the CLIGEN model (Nicks et al., 1995; PRISM Climate Group Oregon State University, 2004; Srivastava et al., 2019) derived from long-term observations at nearby weather stations. Additionally, users have the option to correct precipitation and temperature based on monthly and annual PRISM maps (PRISM Climate Group Oregon State University, 2004). The other model input requirements for WEPPcloud-PEP are soil burn severity (unburned, low, moderate, and high severity), soil texture, and topography. The most important model parameters related to soil for hillslope soil erosion are interrill (K_i) and rill (K_r) erodibility, and effective hydraulic conductivity for water infiltration (K_e), and for channel erosion, the critical shear stress (τ_c) (Elliot & Hall, 2014). These parameters are predefined in the model in default soil files based on the soil texture from post-wildfire field measurements (Robichaud et al., 2007). The model uses a 10 m DEM and breaks up large watersheds into individual sub-watersheds using TOPAZ (Garbrecht & Martz, 1997), and hillslopes are treated as one-dimensional paths using average hillslope values. The runoff and sediment yield is computed using daily time steps.

In this study, we used WEPPcloud-PEP with similar assumptions that would be used by land managers after a fire, and we compared the predicted mean annual sediment erosion volumes from the model to our observed sediment volumes from the airborne lidar difference in Van Tassel. Erodibility parameters were chosen using the model default options based on the soil burn severity map of the watershed. We used 30 yr of weather data generated by the CLIGEN model based on the historical weather data observed at a nearby station (MT WILSON FC 338B CA 46006 0) with PRISM adjustments to account for changes in precipitation as a function of elevation. The model delineates hillslope sub-basins as well as channel polygons. Here the channel and sub-basins were defined using a minimum channel length of 100 m and a critical source area of 1×10^5 m^2. The hillslopes were divided into sub-catchments with unique ID numbers, and a total mass of sediment erosion (tonnes) was calculated for all sub-catchments and channels. We used a literature-derived bulk density estimate of 1.14 Mg/m^3 (Robichaud et al., 2008) to convert to a volume of erosion (m^3). In order to compare the airborne lidar difference map and the model, the lidar data were extracted and summed from the same hillslope and channel polygons that were used in the modeling. We note that the WEPPcloud-PEP hillslope polygons contain small channels with debris flow activity that are not represented in the model.

4. Results

4.1. Processes, Patterns, and Controls on Post-Wildfire Sedimentation

Our airborne lidar error analysis using stable features showed a maximum elevation change <5 cm on paved roads and up to 12 cm on dirt roads (Figure 2). Reports from the ground control surveyed with GPS show that maximum uncertainty was <19.6 cm in the LA County lidar flights (Jennings & Powers, 2015) and <12.7 cm for the USGS lidar flights (Burroughs & Silvia, 2018). Our observations of stable features

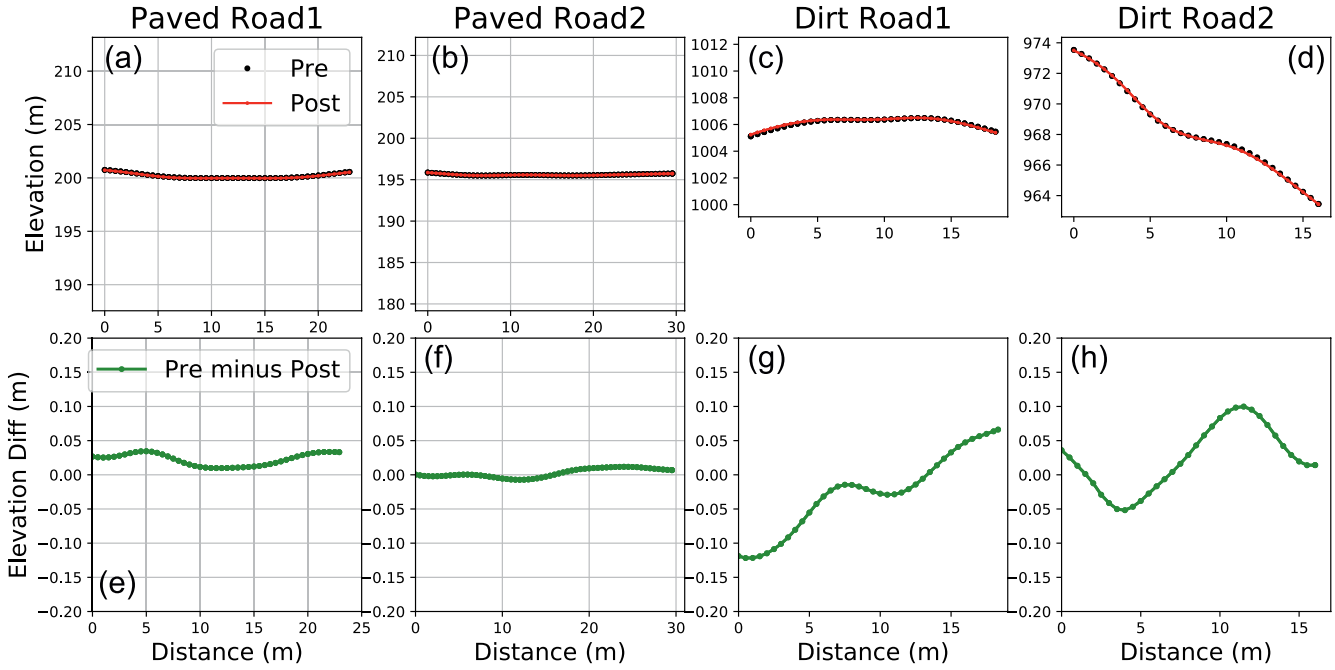

Figure 2. Difference in elevation between selected pre- and post-erosion airborne lidar data points at four relatively stable road locations. (a–d) Elevation of original points. *Note*. The aspect ratio of the elevation-distance plots (top row) is determined by forcing equal spacing on both axes to prevent vertical exaggeration; therefore, the plot sizes vary. (e–h) The elevation difference between the pre- and post-erosion airborne lidar.

(Figure 2) show a maximum registration uncertainty in stable areas of 12 cm and the average uncertainty due to roughness and point density (LoD_{95}) from Equation 2 was ±1.2 cm. Based on these factors, we chose a conservative minimum LoD of ±15 cm for the airborne lidar. The TLS LoD was established as the root-mean squared error of the registration error of the scan positions ±2 cm and the average uncertainty due to roughness (±1 cm from Equation 2); therefore, we used ±3 cm as the TLS LoD (Rengers & McGuire, 2018).

Using the multiple scales of lidar data (airborne and terrestrial), we gained insight into the processes operating at the hillslope and watershed scales (Figure 3). We found that hillslope change in the TLS plot was below the LoD of the airborne lidar, despite observations of substantial change using TLS (Figure 3). For example, in the airborne lidar data in the Las Lomas watershed, it appears that most of the topographic change takes place in the channelized areas (Figure 3a). However, after the first rainy season, the TLS data show substantial hillslope change. The total volume eroded from interrill areas (18.1 m^3) was on par with rilling erosion (19 m^3), and both of these were larger than the estimated post-wildfire dry ravel (4.7 m^3) (Table 2). The first and last TLS surveys record the surficial response to all of the runoff-producing storms in the 2016–2017 winter (Figure 4a), and the net erosional volume (m^3) divided by the survey area (m^2) is 4.7 cm. Note the Gaussian filtering techniques requires subsampling the sides of the area, so the total area used for this calculation was 770 m^2.

In the Van Tassel watershed, airborne lidar data show hillslopes are net erosional and the source of most of the sediment that moves through the channel network (Figures 4b and 5). Because of the large portion of the hillslopes that fell below the LoD (Figure 4b), we also estimated a potential volume from those areas < the airborne lidar LoD and <45° using the net hillslope erosion (4.7 cm) from the TLS plot. With this approach, the potential volume of sediment eroded from the hillslope areas below the airborne lidar LoD is 1.1×10^5 m^3, which is approximately half of the net volume of hillslope erosion obtained from the airborne lidar (2.25×10^5 m^3) (Figure 5). The headwater channels with contributing drainage areas between 1×10^3 and 1×10^5 m^2 also show net erosion, whereas at slightly larger scales 1×10^5 to 3×10^6 m^2, erosion and deposition are fairly balanced, narrowly resulting in net erosion (Figure 5). Finally, at the largest channel scales (>3×10^6 m^2) where the channel is exiting the mountain front, the channels become dominantly depositional (Figures 4b and 5). This pattern can be visualized along the longitudinal profile of the largest channel flowing through the Van Tassel watershed (Figure 6). The three distinct zones of sedimentation

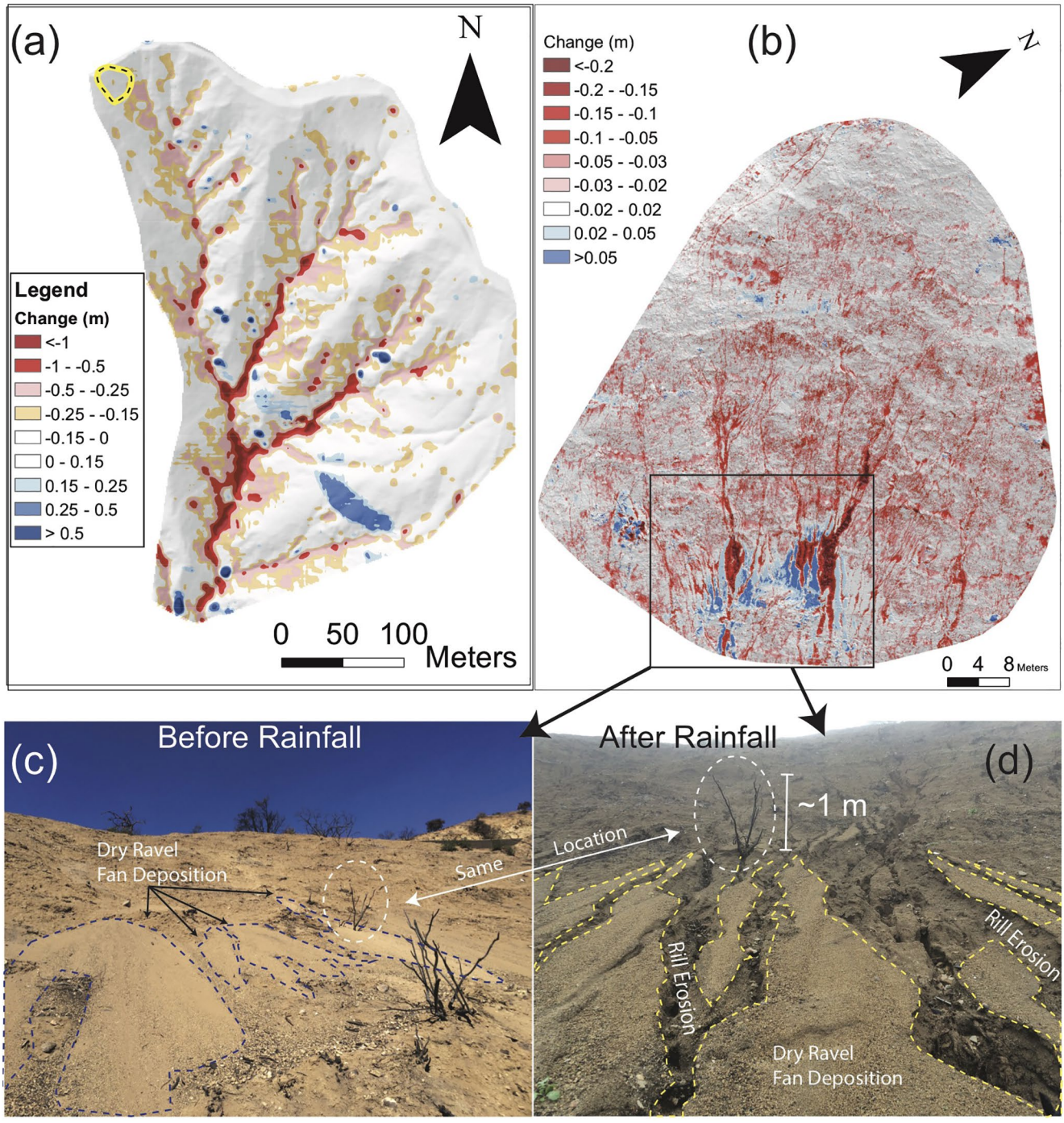

Figure 3. (a) Airborne lidar surface change map of the Las Lomas watershed (December 2015 to August 2017, location shown in Figure 1b), where blue shades represent deposition (positive values) and red shades represent erosion (negative values). The yellow polygon with dashed black line indicates the location and footprint of the TLS survey area in (b). *Note*. A large blue swath in the bottom right is a post-fire anthropogenic disturbance. (b) Terrestrial lidar surface change map (November 2016 to January 2017) showing erosion and deposition at a small hillslope in the Las Lomas watershed after rainfall (site location is shown as yellow polygon in (a) and as star in Figure 1). (c) Photo of the hillslope on September 9, 2016, after wildfire and before rainfall (Photo credit L. McGuire). The lighter colored sediment composing dry ravel fans in the foreground is outlined in a blue dashed line. A white dashed circle indicates the same burned stem in each photo. (d) Photo of the hillslope on January 5, 2017 after several rainstorms (Photo credit L. McGuire). Rills have incised the dry ravel fans. The remaining fan surface is outlined in a dashed yellow line.

Table 2
Erosion Characteristics of the Terrestrial Lidar Hillslope Plot

Metric	Jul. 23, 2016–Nov. 19, 2016	Nov. 19, 2016–Jan. 5, 2017	Jan. 5, 2017–Feb. 22, 2017
Dry ravel deposition (m^3)	4.7	n/a	n/a
Total rill erosion (m^3)	n/a	5	14
Total interrill erosion (m^3)	n/a	4.6	13.5
Dry ravel Deposition per area (m)	0.005	n/a	n/a
Rill erosion per area (m)	n/a	0.006	0.018
Interrill erosion per area (m)	n/a	0.005	0.017

are shown in the longitudinal profile (erosion dominant, mixed erosion/deposition, and deposition dominant) (Figure 6a). A channel slope angle of 6° appears to broadly delineate areas of erosion (>6°) versus areas of deposition (<6°) (Figure 6b).

Because lidar interpretations vary based on the grid resolution (e.g., Kasprak et al., 2019), we examined the sensitivity of the sediment budget to the airborne lidar data grid resolution by increasing the grid resolution to 1 m. We found that the observed patterns were consistent, varying from 0.4% for the hillslopes > the LoD to a maximum of 4.8% for channels 1×10^5 to 3×10^6 m^2. The absolute differences in volume were small, ranging from 50 to 1,000 m^3.

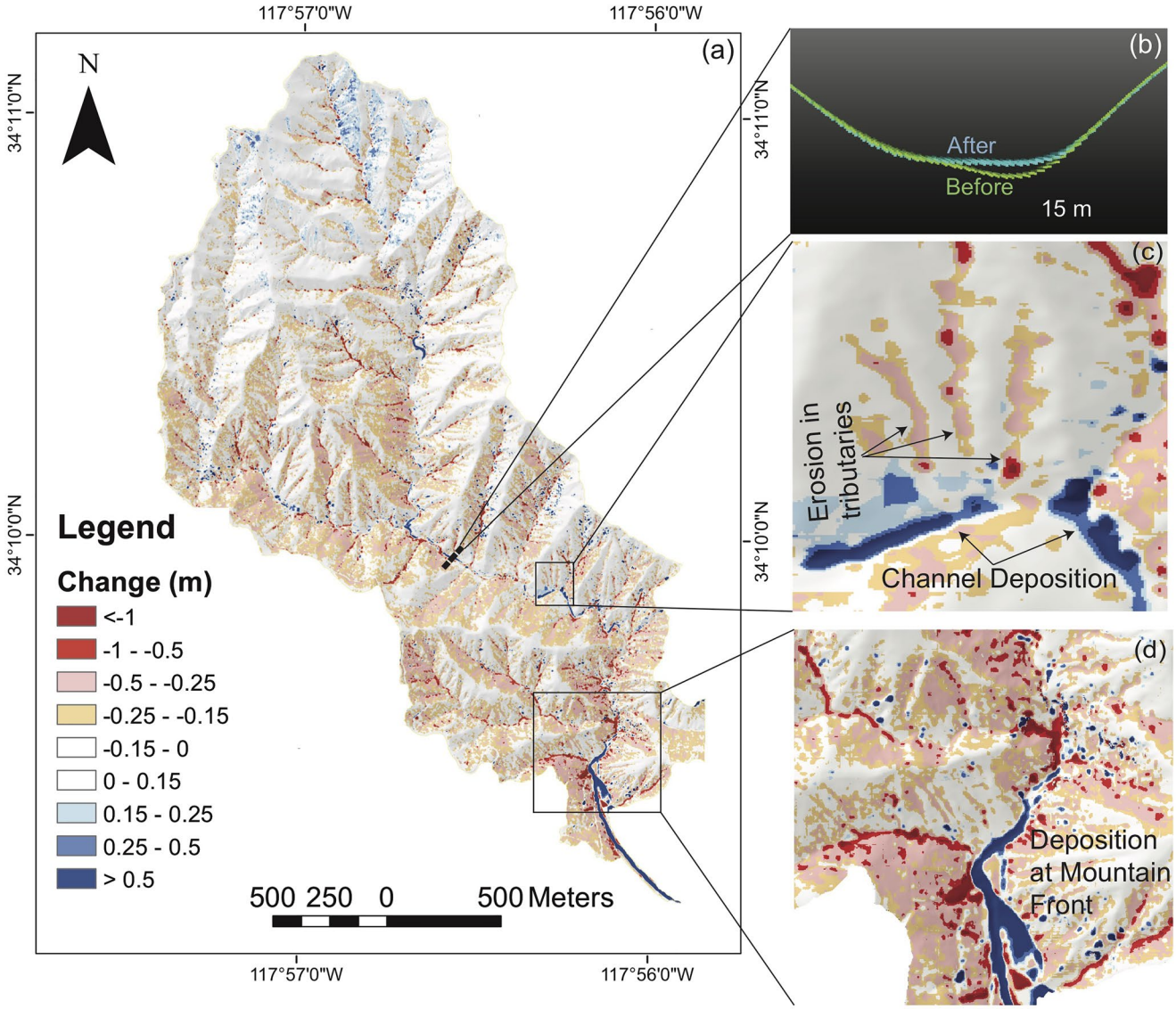

Figure 4. (a) The airborne lidar surface change map for the Van Tassel watershed. (b) Cross section taken from the pre- and post-erosion airborne lidar point clouds, showing tight registration on channel banks with little erosion, and deposition within the channel. (c) Enlargement on a portion of the airborne lidar change map where tributary channels are eroding sediment and deposition is occurring within the trunk channel. (d) Enlargement on a portion of the airborne lidar change map where the channel is exiting the mountain front and sustained channel deposition occurs.

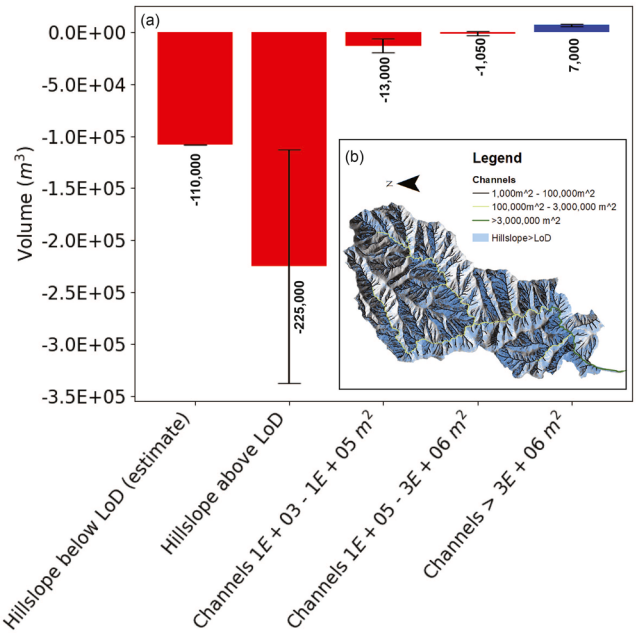

Figure 5. (a) Sediment budget estimated from airborne lidar binned by the upstream contributing drainage area. The numbers near the bars represent the net volume (m^3) in each landform category. Negative numbers indicate erosion. For the portion of the hillslope < the airborne lidar LoD and <45°, we multiplied the average TLS-derived hillslope erosion rate by the area to estimate the hillslope erosion (labeled as Hillslope below LoD (estimate)). Error bars indicate ±0.15 (m). (b) Location map showing each landform category, overlaying a hillshade map.

Within the channel reaches, we used HAND to analyze the sources of erosion at three distinct elevations zones, defined with respect to the height above the nearest channel bed (Figure 7). The active bed (<0.5 m above the pre-fire channel thalweg) had a net erosional volume of 6,500 m^3, which accounts for approximately 3% of the net volume eroded from the watershed (upstream of the canyon mouth). The channel banks (0.5–3 m above the pre-fire channel thalweg) had a net erosional volume of 9,300 m^3, which accounts for approximately 4% of the net volume eroded from the watershed (upstream of the canyon mouth). The remaining 93% of the net erosional volume (2.16×10^5 m^3) within the watershed was derived from hillslopes above the channel banks (areas located >3 m above the pre-fire DEM elevation). Moreover, we find that the natural logarithm of α shows a trend in the net channel elevation change ($R^2 = 0.48$) (Figure 8a). Portions of the channel with the lowest α values show deposition, and as α increases the channel becomes primarily erosional. We did not observe a strong trend in net channel change with distance downstream from tributaries, indicating that tributary input of sediment does not appear to substantially change the location of channel erosion or deposition over the time period of our lidar change detection (Figure 8b).

Sediment yield varied in complex ways with respect to slope and upstream contributing drainage area. Although the eroded sediment volume increases with drainage area (Figure 9a) the sediment yield is high at drainage areas $<1 \times 10^3$ m^2. It is roughly at this drainage area where the slope-area curve attains an approximate power-law scaling, that is, where channels begin (Figure 9b). The sediment yield then plateaus until reaching a contributing area of approximately 2×10^5 m^2, where it briefly declines with increased channel deposition before increasing again at the largest contributing drainage areas.

4.2. Model Testing

In a comparison of the observed volume from the airborne lidar with predicted volumes from four equations developed in previous studies, we found that the results varied over three orders of magnitude and Equation 6 (Gartner et al., 2014) performed the best (Figure 10). For the volume comparison in each sub-basin, we also included estimates of the hillslope sediment in areas that are < the LoD (Figure 10a). We fit a trend line to the observed data with the hillslope estimate from the TLS survey to obtain an expression for the observed volume (V) (m^3) of sediment transported through any point in the landscape as a function of drainage area (A) (m^2) (Figure 10a) using:

$$V = fA^{0.93} \tag{11}$$

where $f = 0.19$ ($m^{1.14}$). Note that the observed volumes are thresholded by removing areas of the watershed below the LoD. This relationship is directly comparable in form to Equation 10. Equation 11 predicts a higher volume of sediment erosion with increasing drainage area than the equation derived by Nyman et al. (2020) (Equation 10; Figure 10), but is similar to an equation with the same form developed by Pelletier and Orem (2014) that had a similar exponent (0.98).

To quantify the offset between the observed (plus the estimated) volumes and the volumes predicted from Equation 6, we compared the difference in best-fit lines with a 1:1 line (Figure 10b). There was a bias toward higher predicted volumes for both the observed data and the observed data with the TLS hillslope estimate (slopes of the best-fit lines were 1.72 and 1.12, respectively).

A comparison of the airborne lidar volumetric measurements with the process-based WEPPcloud-PEP model shows differences between the observed and predicted volumes on hillslopes and channels. In the

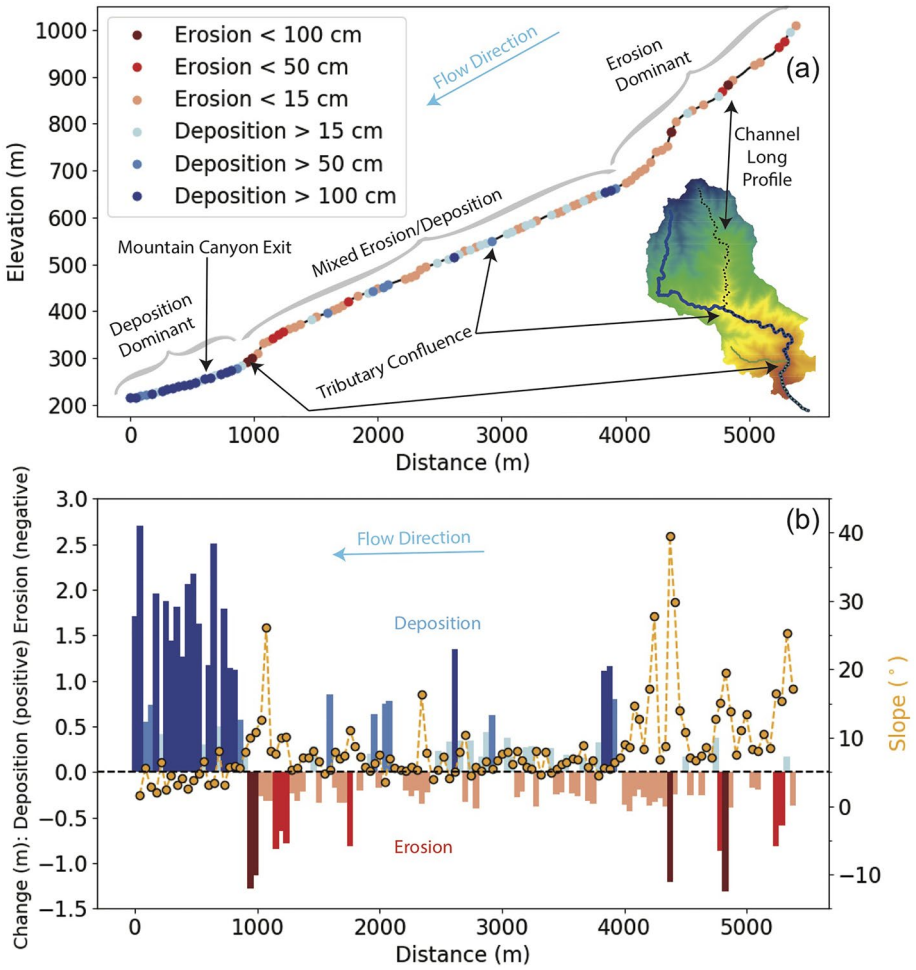

Figure 6. (a) Longitudinal profile showing the elevation as a function of distance from the watershed outlet for the longest channel in the Van Tassel study watershed (dashed line). Colored dots along the profile show the erosion/deposition magnitude, and areas without a dot are below the level of detection. Arrows indicate the location on the longitudinal profile where there is a confluence between the primary drainage (dashed line) and large tributaries (dark blue and dark green lines). The reference watershed is colored by elevation, with high elevations (cool colors) transitioning to low elevations (warm colors). (b) Plot of deposition and erosion along the longitudinal profile as a function of distance (primary *y*-axis) as well as the local slope along the longitudinal profile (secondary *y*-axis). Dashed line highlights indicates where erosion and deposition = 0 m.

hillslope areas, the WEPPcloud-PEP underestimates the observed volumes substantially, and the channel erosion estimates are approximately an order of magnitude larger than the observations (Table 3).

5. Discussion

5.1. Geomorphic Processes and Sediment Redistribution Patterns

Despite the current breadth of data and literature documenting individual sediment transport processes within unique process domains that make up a sediment cascade system in a burned watershed (Moody et al., 2013; Robichaud, 2005; Robichaud et al., 2016; Santi & Rengers, 2020; Shakesby & Doerr, 2006), field studies that examine the coupling of sediment supply, routing, and storage at the watershed scale remain rare (Nyman et al., 2020), making it difficult to predict the watershed scale consequences of sediment redistribution after a wildfire. The sediment dynamics are particularly confounding in portions of watersheds that are subject to both debris flow and fluvial processes, which have different erosion/deposition mechanics (Nyman et al., 2020). Understanding the spatial and temporal redistribution of sediment at the

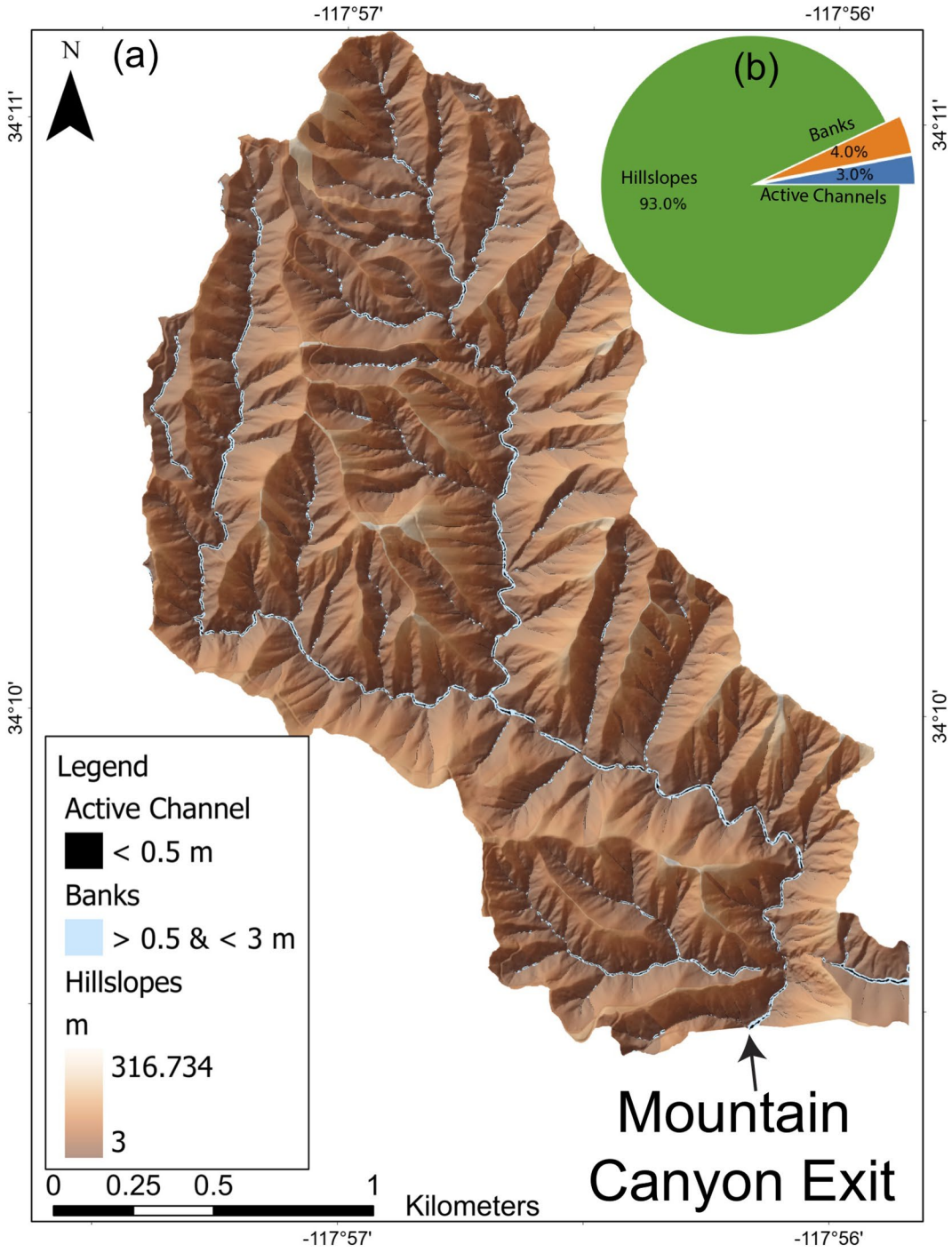

Figure 7. (a) Map showing the vertical height above nearest drainage (HAND) (m). (b) Pie chart showing the net erosion in the active channel (3%) (<0.5 m above nearest drainage), the channel banks (4%) (>0.5 and <3 m above nearest drainage), and the hillslopes is 93% (>3 m above nearest drainage).

watershed scale after wildfire is critical to preparing for the hazards associated with post-wildfire erosion and deposition in a watershed.

Consequently, our first research question focused on understanding the processes that lead to erosion and deposition partitioning throughout a landscape. At the watershed scale, the airborne lidar data show that the majority of erosion comes from hillslopes, and deposition occurs in low-sloping portions of the main

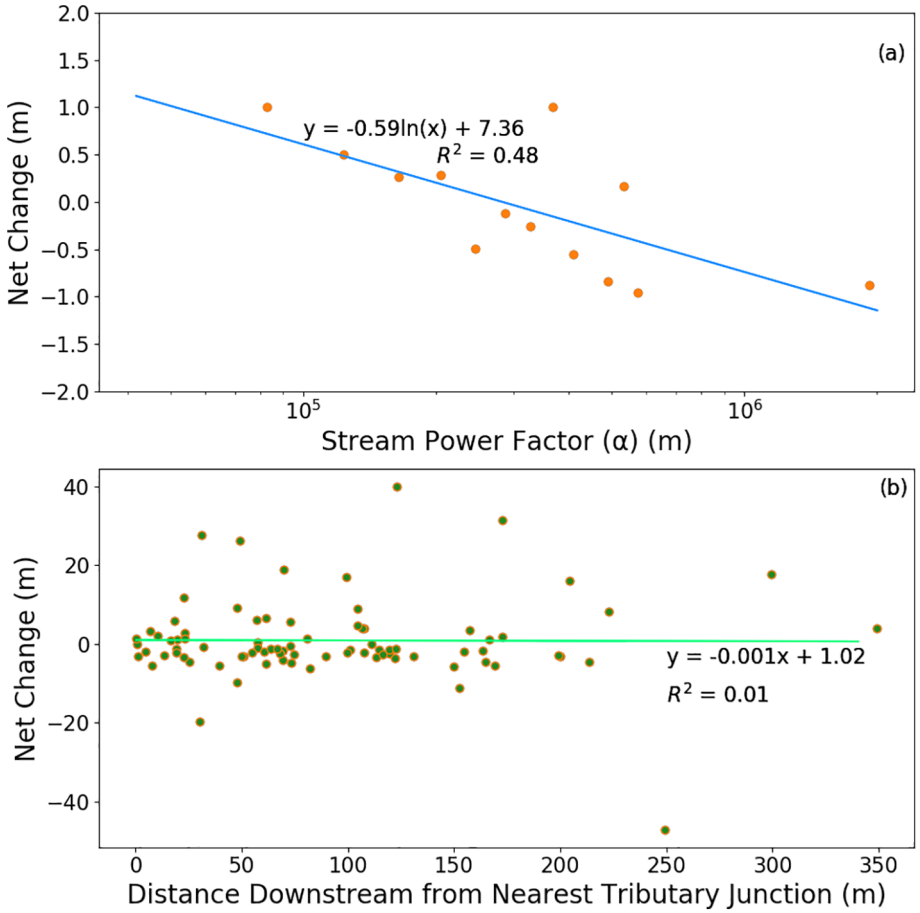

Figure 8. (a) Comparison of the average cross section change versus the stream power topographic factor (α) binned by upstream contributing drainage area. (b) Comparison of the average cross section change versus the distance downstream from the nearest tributary with a drainage area $>1 \times 10^5$ m^2.

channels (Figure 4b). However, the level of detection of the airborne lidar limits the amount of landscape change visible at the hillslope scale (Figure 4b). We filled in this data gap with TLS data (Figure 3) on a small hillslope. The TLS data show a complex pattern of dry-ravel, dispersed raindrop-driven and overland flow erosion, concentrated rill erosion, and sediment deposition (Figure 3), similar to observations in other steep burned sites (e.g., Guilinger et al., 2020). At the TLS site, the erosion was from a combination of disperse interrill erosion, dry ravel, and rill erosion (Table 2). This shows that airborne lidar data are not sufficiently detailed to completely describe the shallow sediment redistribution processes at work on hillslopes with the smallest drainage areas. Using the TLS data to estimate the potential erosion in areas <the airborne lidar LoD and <45°, we found that undetected hillslope erosion could be approximately 50% larger than the volume measured by airborne lidar (Figure 5). Consequently, using airborne lidar data and TLS together can help show the overall patterns of sediment redistribution within the watershed.

Prior studies have recognized that watershed size strongly influences post-wildfire sediment delivery (Lavé & Burbank, 2004). Therefore, to account for scaling differences, we examined sediment yield throughout the study area within the context of the slope-area curve (Figure 9). The slope-area curve should reflect process dominance over geologic time scales, which may or may not match process dominance over short time scale of this study. Fluvial channels begin near a drainage area of 1×10^3 m^2 (Rengers et al., 2019), and the sediment yield is high up to this drainage area. At the point where we expect fluvial processes to start to dominate, the sediment yield plateaus at drainage areas of 2×10^3 to 2×10^4 m^2 because the volume of sediment being eroded increases linearly with contributing drainage area for this portion of the landscape (Figure 9). A slope break for drainages near 2×10^5 m^2 (Figure 9) results in deposition within fluvial

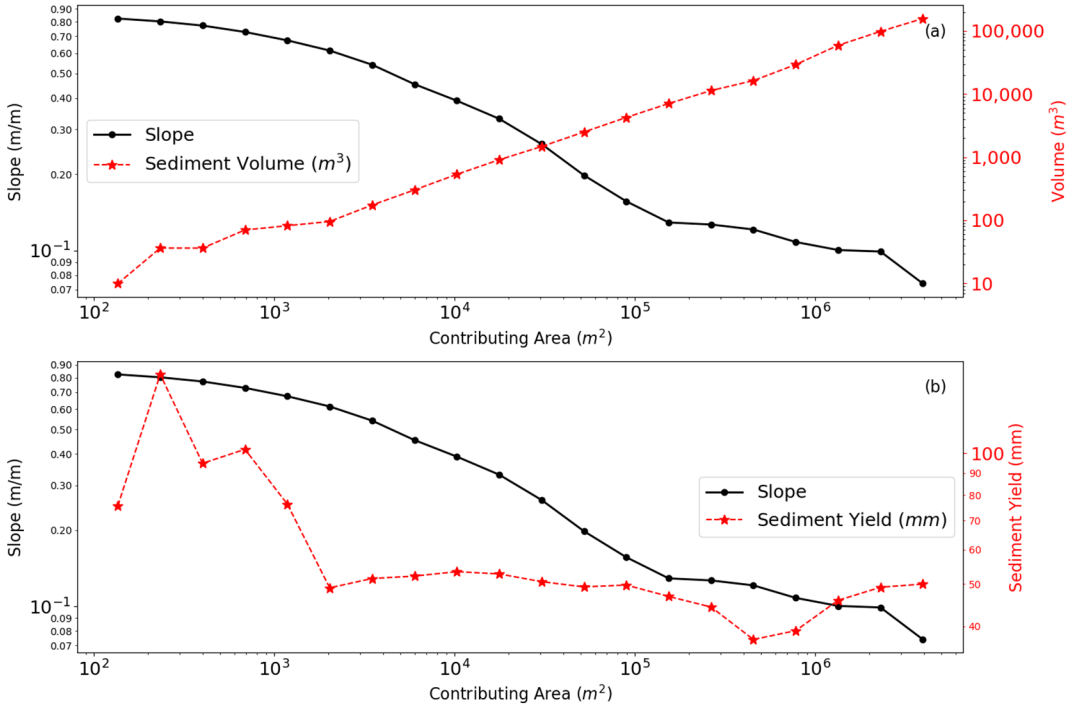

Figure 9. Slope-area curve compared to (a) the volume of sediment passing through each pixel and (b) the sediment yield at each pixel.

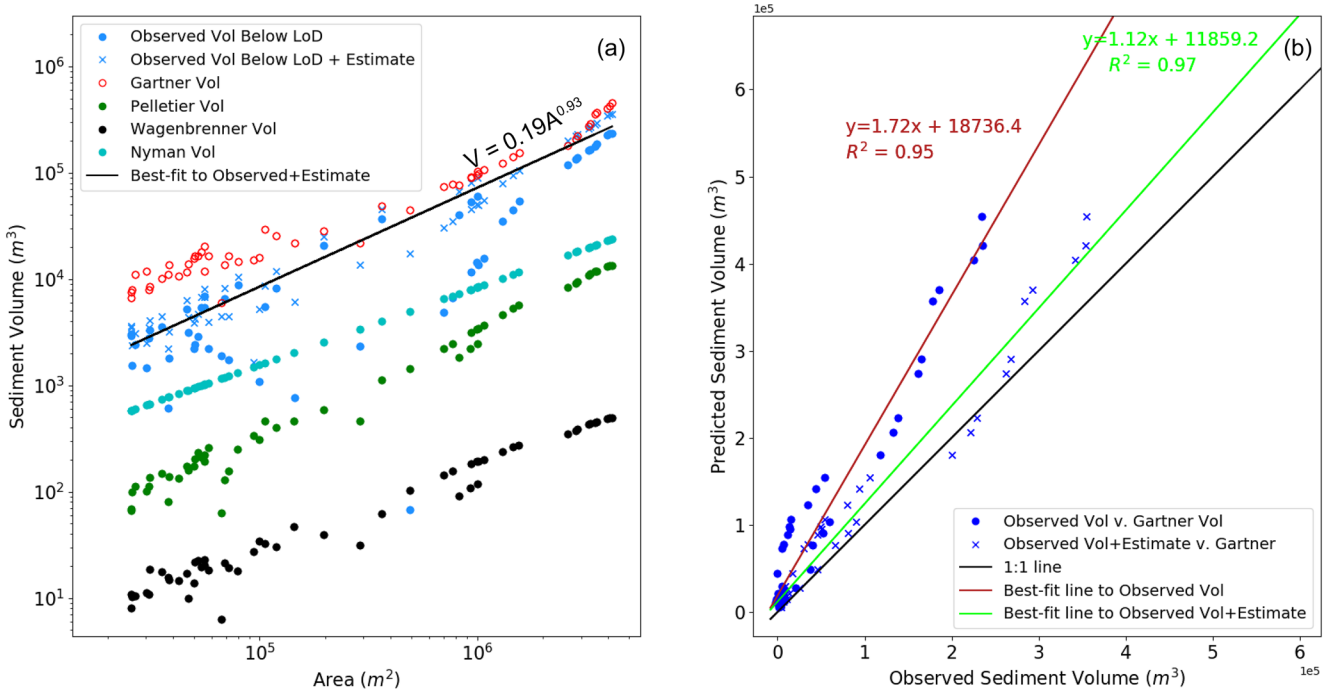

Figure 10. (a) Comparison between measured airborne lidar sediment volume and estimated sediment volume from Equations 6–10. In addition, we applied the erosion rate from the TLS plot to portions of the landscape that were <the airborne lidar LoD and had a slope <45°, and that volume is labeled as "Observed Vol + Estimate" on the plot. The equations used to model volume are labeled in the plot with the first author surnames: Gartner (Equation 6), Pelletier (Equation 7), Wagenbrenner (Equations 8-9), and Nyman (Equation 10). (b) A one-to-one comparison between the lidar observations and the volume predictions using Equation 6. Best-fit lines have been fit to both the observed volume and the observed volume with the additional hillslope estimate from the TLS plot. The points labeled as "Observed Vol + Estimate" represent the same erosion estimate as described for (a).

Table 3
WEPP Volume Estimates Compared to the Observed Airborne Lidar Volume in the Same Areas

Region	WEPP sediment volume (m^3)	Lidar sediment volume (m^3)
Hillslope	14,500	230,000
Channel	23,500	2,300
Total (sum)	38,000	232,300

Note. The hillslope erosion in WEPP is limited to overland flow erosion only.

channels, and this can be seen spatially (Figures 4b, 5, 6, and 9b). At the highest drainage areas, more eroded sediment passes through the channel system than is deposited (Figure 9). The sediment erosion/deposition patterns observed in this study and contextualized using slope-area plots could be used to guide decision making in similar terrain. For example, the slope-area curve shows that sediment yield is highest on hillslopes before channelization. Likewise, we see that at large drainage areas, deposition occurs in local reaches with low slopes, and mapping of drainage area and slope could help managers to identify portions of the landscape susceptible to rapid deposition. This could result in actions for overall mitigation (e.g., deWolfe et al, 2008) such as planning for deposition below bridges, in culverts, or near utility crossings.

The most complex patterns of erosion and deposition were found within the channel networks. An analysis of sedimentation patterns for the longest channel in the Van Tassel watershed shows erosion dominance near the top of the catchment and deposition dominance near the base of the watershed with a mixed zone of erosion and deposition in the middle portion (Figure 6a). The mixed erosion and deposition area appears to be driven by changes in local slope, often with deposition occurring when the local slope drops below 6° (Figure 6b). We used a HAND analysis to identify the source of material for the channel change using our three defined zones: active channel, channel banks, and hillslopes. Unlike other observations that show most of the debris flow erosion in the channel network coming from the active channel bed and banks (Santi et al., 2008; Ellett et al., 2019), we found that over 93% of the net erosional volume came from hillslopes (Figure 7). However, the differences in observations may be tied to the methodology of measurement. For example, field observation at our site showed that in some locations dry ravel moved directly into channels. Thus measurements of channel erosion using an approach similar to Santi et al. (2008) may include dry ravel deposits in channels that are subsequently eroded as channelized erosion. Consequently, differences in accounting in a sediment budget could lead to estimates of more channel erosion than we calculate here.

In addition, it appears that the erosion/deposition within the channelized network can be partially explained by a topographic factor (α) using a stream power approach (Equation 5). Stream power should not be expected to describe debris flow erosion/deposition well because the mechanics of debris flow movement differ significantly from water-dominated flows. However, because the Van Tassel watershed experienced both floods and debris flows over the time between the airborne lidar surveys (Michel et al., 2019), it appears that a stream power approach can be used to explain general trends in channel sedimentation (Figure 8a). Stream power also appears to have a stronger correlation with net channel change than the downstream distance to tributaries (Figure 8a). This result may be due to the fact that the lidar observations in this study allow for an entire rainy season to rework sediment, and it is possible that after a single event where tributaries input large sediment volumes, the downstream distance of a cross-section to a tributary junction may show a stronger correlation with net channel change. Consequently, because the topographic factor (α) can be calculated from a lidar DEM prior to any rainfall, it could be explored as a rough analytical tool for erosion/deposition planning purposes, but more datasets would be required to assess this approach. Furthermore, caution would be required with this approach in areas where there is substantial erosion of channel banks outside of pre-defined cross sections.

5.2. Sediment Volume Observations Versus Predictions

Accurate estimates of potential post-wildfire debris flow volumes are critical for appropriate design standards for debris retention structures (Prochaska, Santi, & Higgins, 2008), assessing temporal changes in channel capacity due to sedimentation, and constraining inputs needed to run debris flow inundation models (Griswold & Iverson, 2008; Iverson et al., 1998; Schilling, 1998). In addition, post-wildfire sediment volume estimates are important for assessing post-wildfire sedimentation problems in municipal water supply reservoirs (Robichaud et al., 2014; Robinne et al., 2016). Because of the importance of accurately estimating sediment volumes, our second research question focused on how the observed erosion volumes from the Van Tassel watershed compared to predictions. We tested four empirical models that have been developed

to estimate sediment erosion volumes and compared the results against the lidar observations. We found the closest fit between the observed volume from the airborne lidar and predicted volumes using Equation 6 (Gartner et al., 2014). In a direct comparison of Equation 6 and the lidar observations, we see a tendency toward overprediction, however, this may also be biased by the LoD of the lidar data (Figure 10b). If we add an estimate of hillslope erosion for areas < the airborne lidar LoD and <45°, assuming similar hillslope erosion rates as the TLS plot, we see a closer fit to the equation. The data used to develop Equation 6 were obtained from the Transverse Ranges in southern California, which may help to explain the close fit. The estimated sediment volumes from Equations 7 to 10 deviated further from the observations, which might be expected because they were developed from data in different regions. Because empirically-derived equations will inherently be fit to regional properties (e.g., climate, geology, soils, weathering, tectonic history, etc.), it is likely that the best approach for estimating post-fire sediment volumes will be either (1) to develop a suite of regional models that can be used for specific areas of interest, or (2) to develop a mechanistic model that can be adjusted for regional differences.

The general sources of uncertainty in the volume models include the bulk density that was assumed and used to estimate the sediment volume in Equations 7–9, and the estimate of ground cover in Equation 8. Specific sources of uncertainty in Equations 7–10 arise due to differences in the ecosystems, geologic settings, and climates where the datasets underlying those equations were obtained. The data used to develop Equations 8 and 9 were obtained from watersheds smaller than 1.2 km^2 and did not contain many observations of debris flows, unlike the study watershed. At another extreme, Equation 7 was developed in a watershed that was primarily influenced by debris flows. Finally, Equation 10 was developed using hillslope erosion estimated through modeling, and channel change estimated with observational cross-section data. The lack of detailed hillslope erosion data may factor into the observed differences with our lidar observations.

The process-based model comparison (WEPPcloud-PEP) underestimates the average annual sediment volume predictions for hillslopes compared to the lidar observations, and overestimates the volume results for channel regions (Table 3). The dissimilarity in channel and hillslope prediction and observations are likely related to dry ravel and debris flow events in small catchments (Figure 4b), which WEPP was not designed to predict. WEPP was designed to simulate surface erosion from rill and interrill erosion. Other potential sources of error in the modeling are the default erodibility parameters used to estimate erosion in the watershed, the bulk density estimates used to estimate the volume, and differences in observed versus modeled rainfall. However, with respect to rainfall, the CLIGEN weather module used in WEPPcloud-PEP appears to match the overall observed rainfall trends closely. The CLIGEN-estimated annual precipitation is 880 mm, which compared well with the site annual precipitation (600–950 mm). Some rainfall intensity recurrence intervals are reported directly in WEPPcloud-PEP, and we found that the reported 10-min rainfall intensity at the 2-yr (92 mm/h) and 5-yr (110 mm/h) recurrence intervals were near or slightly higher than the ranges of 10-min rainfall intensities reported by NOAA Atlas-14 (NOAA, 2020) at the same recurrence intervals (55–80 and 72–106 mm/h). The maximum observed rainfall intensities at the site (Table 1) are within the range of average annual 10-min (42–62 mm/h) and 15-min (34–50 mm/h) rainfall intensities estimated by NOAA Atlas-14 (NOAA, 2020), suggesting that the rainfall conditions at the site were close to the average annual conditions.

The observed erosion from the Van Tassel watershed shows that erosion following wildfire can be a substantial contributor to long-term erosion rates. The average landscape lowering obtained from the airborne lidar data in the Van Tassel watershed is 5.5 ± 0.9 cm. This results in an average erosion rate of 0.9 mm/yr assuming an average wildfire recurrence interval of 50–80 yr (Keeley, 1981; Minnich, 1983; Zedler, 1995) for this region and a similar erosional response following each wildfire event. That rate is within the range of reported bedrock erosion rates (0.036–2.2 mm/yr) in the San Gabriel Mountains (Neely & DiBiase, 2020), suggesting that post-wildfire erosion is an important mechanism for moving sediment out of the mountains and helping to maintain shallow soils and bedrock channels in this mountain chain.

6. Conclusion

We have explored the post-wildfire processes and patterns of erosion and deposition using terrestrial and airborne lidar. Our first research question asked how erosion and deposition were partitioned across the landscape. At the watershed scale, most erosion is derived from hillslopes, and the TLS data show that hillslope erosion is a mix of dry ravel, interrill erosion, and rill erosion. The channel system, by contrast, conveys hillslope sediment, provides additional sediment via channel bed and bank erosion, and can act as a depositional sink. This study shows empirical relationships between erosion/deposition using slope-area and stream power. These patterns could be used as a first cut to predict areas of concern for managers interested in identifying erosion or deposition before post-wildfire rainstorms. Our second research question asked how well existing models predict post-wildfire erosion volumes. Generally, the post-wildfire debris flow volume model proposed by Gartner et al. (2014) best predicted erosional volumes. The WEPPcloud-PEP model underestimated sediment yields on hillslopes, but overestimated sediment yield in channels compared to the observed airborne lidar. We attribute these differences to the debris flow and dry ravel erosion, which the model was not designed to simulate, as well as the fact that the model was not specifically calibrated to the study watershed. Consequently, this study shows both the generalized spatial distribution of post-wildfire erosion and deposition throughout a landscape, and serves as a test case for model validation. Results further highlight the important contribution to long-term erosion rates made by erosion in the immediate aftermath of wildfire.

Data Availability Statement

Airborne lidar data are available online through the USGS 3D Elevation Program https://www.usgs.gov/core-science-systems/ngp/3dep, and the terrestrial lidar data are available in McGuire and Rengers (2019).

Acknowledgments
This work was supported by the USGS landslide hazards program. Any use of trade, firm, or product names is for descriptive purposes only and does not imply endorsement by the U.S. Government. We would like to thank Dimitri Lague for helpful conversations about point cloud differencing. We also acknowledge helpful manuscript comments from Amy East, Joel Sankey, Roman DiBiase, Steve DeLong, Corina Cerovski-Darriau, and an anonymous reviewer.

References

Arocena, J., & Opio, C. (2003). Prescribed fire-induced changes in properties of sub-boreal forest soils. *Geoderma*, *113*(1), 1–16. https://doi.org/10.1016/S0016-7061(02)00312-9

Benda, L. (1990). The influence of debris flows on channels and valley floors in the Oregon Coast Range, USA. *Earth Surface Processes and Landforms*, *15*(5), 457–466. https://doi.org/10.1002/esp.3290150508

Benda, L., & Dunne, T. (1997). Stochastic forcing of sediment supply to channel networks from landsliding and debris flow. *Water Resources Research*, *33*(12), 2849–2863. https://doi.org/10.1029/97wr02388

Bennett, G., Molnar, P., McArdell, B., & Burlando, P. (2014). A probabilistic sediment cascade model of sediment transfer in the Illgraben. *Water Resources Research*, *50*(2), 1225–1244. https://doi.org/10.1002/2013WR013806

Bernard, T. G., Lague, D., & Steer, P. (2020). Beyond 2D inventories: Synoptic 3D landslide volume calculation from repeat LiDAR data. *Earth Surface Dynamics Discussion*. [preprint]. https://doi.org/10.5194/esurf-2020-73

Brodu, N., & Lague, D. (2012). 3d terrestrial lidar data classification of complex natural scenes using a multi-scale dimensionality criterion: Applications in geomorphology. *ISPRS Journal of Photogrammetry and Remote Sensing*, *68*, 121–134. https://doi.org/10.1016/j.isprsjprs.2012.01.006

Brogan, D. J., Nelson, P. A., & MacDonald, L. H. (2017). Reconstructing extreme post-wildfire floods: A comparison of convective and mesoscale events. *Earth Surface Processes and Landforms*, *42*(15), 2505–2522. https://doi.org/10.1002/esp.4194

Brogan, D. J., Nelson, P. A., & MacDonald, L. H. (2019). Spatial and temporal patterns of sediment storage and erosion following a wildfire and extreme flood. *Earth Surface Dynamics*, *7*(2), 563–590. https://doi.org/10.5194/esurf-7-563-2019

Bull, L., & Kirkby, M. (1997). Gully processes and modeling. *Progress in Physical Geography*, *21*(3), 354–374. https://doi.org/10.1177/030913339702100302

Bull, W. B. (1991). *Geomorphic responses to climatic change* (575 pp.). New York, NY: Oxford University Press.

Burroughs, J., & Silvia, E. P. (2018). *USGS California Fault Zone LiDAR Technical Data Report, Tech. Rep*. Corvallis, OR: Quantum Spatial.

Busse, M. D., Shestak, C. J., Hubbert, K. R., & Knapp, E. E. (2010). Soil physical properties regulate lethal heating during burning of woody residues. *Soil Science Society of America Journal*, *74*(3), 947–955. https://doi.org/10.2136/sssaj2009.0322

Cannon, S. (2001). Debris-flow generation from recently burned watersheds. *Environmental and Engineering Geoscience*, *7*(4), 321–341. https://doi.org/10.2113/gseegeosci.7.4.321

Cannon, S., & DeGraff, J. (2009). The increasing wildfire and post-fire debris-flow threat in western USA, and implications for consequences of climate change. In *Landslides-disaster risk reduction* (pp. 177–190). Berlin/Heidelberg: Springer.

Cannon, S., Gartner, J., Parrett, C., & Parise, M. (2003). Wildfire-related debris-flow generation through episodic progressive sediment-bulking processes, western USA. In *Debris-flow hazards mitigation: Mechanics, prediction, and assessment, Proceedings of the Third International Conference on Debris-Flow Hazards Mitigation, Millpress, Rotterdam* (pp. 71–82).

Cannon, S., Gartner, J. E., Rupert, M. G., Michael, J. A., Rea, A. H., & Parrett, C. (2010). Predicting the probability and volume of postwildfire debris flows in the intermountain western United States. *The Geological Society of America Bulletin*, *122*(1–2), 127–144. https://doi.org/10.1130/B26459.1

Cerdà, A., & Doerr, S. H. (2005). Influence of vegetation recovery on soil hydrology and erodibility following fire: An 11-year investigation. *International Journal of Wildland Fire*, *14*(4), 423–437. https://doi.org/10.1071/WF05044

Chandler, C., Williams, D., Trabaud, L., Thomas, P., & Cheney, P. (1983). Fire in forestry. Vol. 1: Forest fire behavior and effects. New York, NY: Wiley.

Chief, K., Young, M. H., & Shafer, D. S. (2012). Changes in soil structure and hydraulic properties in a wooded-shrubland ecosystem following a prescribed fire. *Soil Science Society of America Journal*, *76*(6), 1965–1977. https://doi.org/10.2136/sssaj2011.0072

DeBano, L. F. (2000). The role of fire and soil heating on water repellency in wildland environments: A review. *Journal of Hydrology*, *231*, 195–206. https://doi.org/10.1016/s0022-1694(00)00194-3

DeBano, L. F., Rice, R. M., & Eugene, C. C. (1979). *Soil heating in chaparral fires: Effects on soil properties, plant nutrients, erosion, and runoff, Tech. Rep*. Berkeley, CA: U.S. Forest Service Research Paper (RP-145).

De Graff, J. V. (2018). A rationale for effective post-fire debris flow mitigation within forested terrain. *Geoenvironmental Disasters*, *5*(1), 1–9. https://doi.org/10.1186/s40677-018-0099-z

DeLong, S. B., Prentice, C. S., Hilley, G. E., & Ebert, Y. (2012). Multitemporal ALSM change detection, sediment delivery, and process mapping at an active earthflow. *Earth Surface Processes and Landforms*, *37*(3), 262–272. https://doi.org/10.1002/esp.2234

DeLong, S. B., Youberg, A. M., DeLong, W. M., & Murphy, B. P. (2018). Post-wildfire landscape change and erosional processes from repeat terrestrial lidar in a steep headwater catchment, Chiricahua Mountains, Arizona, USA. *Geomorphology*, *300*, 13–30. https://doi.org/10.1016/j.geomorph.2017.09.028

deWolfe, V. G., Santi, P. M., Ey, J., & Gartner, J. E. (2008). Effective mitigation of debris flows at Lemon Dam, La Plata County, Colorado. *Geomorphology*, *96*(3–4), 366–377. https://doi.org/10.1016/j.geomorph.2007.04.008

DiBiase, R. A., Heimsath, A. M., & Whipple, K. X. (2012). Hillslope response to tectonic forcing in threshold landscapes. *Earth Surface Processes and Landforms*, *37*(8), 855–865. https://doi.org/10.1002/esp.3205

DiBiase, R. A., & Lamb, M. P. (2013). Vegetation and wildfire controls on sediment yield in bedrock landscapes. *Geophysical Research Letters*, *40*(6), 1093–1097. https://doi.org/10.1002/grl.50277

DiBiase, R. A., & Lamb, M. P. (2020). Dry sediment loading of headwater channels fuels post-wildfire debris flows in bedrock landscapes. *Geology*. https://doi.org/10.1130/G46847.1

DiBiase, R. A., Whipple, K. X., Heimsath, A. M., & Ouimet, W. B. (2010). Landscape form and millennial erosion rates in the San Gabriel Mountains, CA. *Earth and Planetary Science Letters*, *289*(1), 134–144. https://doi.org/10.1016/j.epsl.2009.10.036

Dietrich, W., & Dunne, T. (1993). The channel head. In K. Beven, & M. J. Kirkby (Eds.), *Channel network hydrology* (pp. 175–219). Chichester: Wiley.

Ellett, N. G., Pierce, J. L., & Glenn, N. F. (2019). Partitioned by process: Measuring post-fire debris-flow and rill erosion with structure from motion photogrammetry. *Earth Surface Processes and Landforms*, *44*(15), 3128–3146. https://doi.org/10.1002/esp.4728

Elliot, W., Hall, D., & Scheele, D. (1999). *FS WEPP: Forest Service Interfaces for the Water Erosion Prediction Project computer model*. USDA Forest Service, Rocky Mountain Research Station.

Elliot, W. J., & Hall, D. E. (2014). *Disturbed WEPP Model 2.0. Ver. 2014.04.14*. Moscow, ID: U.S. Department of Agriculture, Forest Service, Rocky Mountain Research Station. Retrieved from https://forest.moscowfsl.wsu.edu/fswepp

Fernández, C., & Vega, J. A. (2018). Evaluation of the RUSLE and disturbed WEPP erosion models for predicting soil loss in the first year after wildfire in NW Spain. *Environmental Research*, *165*, 279–285. https://doi.org/10.1016/j.envres.2018.04.008

Fitzpatrick, R. (1980). Effect of forest and grass burning on mineralogical transformations in some soils of Natal. *Soil Irrigation Research Institute Report*, *952*(139), 80.

Flanagan, D. C., Ascough, J. C., Nearing, M. A., & Laflen, J. M. (2001). The Water Erosion Prediction Project (WEPP) model. In *Landscape erosion and evolution modeling* (pp. 145–199). Springer. https://doi.org/10.1007/978-1-4615-0575-4_7

Flanagan, D. C., & Livingston, S. J. (1995). USDA Water Erosion Prediction Project: User summary. Technical Report NSERL Report No. 11.

Florsheim, J. L., Chin, A., O'Hirok, L. S., & Storesund, R. (2016). Short-term post-wildfire dry-ravel processes in a chaparral fluvial system. *Geomorphology*, *252*, 32–39. https://doi.org/10.1016/j.geomorph.2015.03.035

Florsheim, J. L., Keller, E. A., & Best, D. W. (1991). Fluvial sediment transport in response to moderate storm flows following chaparral wildfire, Ventura County, southern California. *The Geological Society of America Bulletin*, *103*(4), 504–511. https://doi.org/10.1130/0016-7606(1991)103<0504:fstirt>2.3.co;2

Fryirs, K. (2013). (Dis) Connectivity in catchment sediment cascades: A fresh look at the sediment delivery problem. *Earth Surface Processes and Landforms*, *38*(1), 30–46. https://doi.org/10.1002/esp.3242

Fuller, I. C. (2008). Geomorphic impacts of a 100-year flood: Kiwitea Stream, Manawatu catchment, New Zealand. *Geomorphology*, *98*(1–2), 84–95. https://doi.org/10.1016/j.geomorph.2007.02.026

Gabet, E. J. (2003). Sediment transport by dry ravel. *Journal of Geophysical Research: Solid Earth*, *108*(B1). https://doi.org/10.1029/2001JB001686

Gabet, E. J., & Dunne, T. (2003). Sediment detachment by rain power. *Water Resources Research*, *39*(1), 1. https://doi.org/10.1029/2001WR000656

Garbrecht, J., & Martz, L. W. (1997). The assignment of drainage direction over flat surfaces in raster digital elevation models. *Journal of Hydrology*, *193*(1–4), 204–213. https://doi.org/10.1016/S0022-1694(96)03138-1

Gartner, J. D., Dade, W. B., Renshaw, C. E., Magilligan, F. J., & Buraas, E. M. (2015). Gradients in stream power influence lateral and downstream sediment flux in floods. *Geology*, *43*(11), 983–986. https://doi.org/10.1130/G36969.1

Gartner, J. E., Cannon, S. H., & Santi, P. M. (2014). Empirical models for predicting volumes of sediment deposited by debris flows and sediment-laden floods in the Transverse Ranges of southern California. *Engineering Geology*, *176*, 45–56. https://doi.org/10.1016/j.enggeo.2014.04.008

Gould, G. K., Liu, M., Barber, M. E., Cherkauer, K. A., Robichaud, P. R., & Adam, J. C. (2016). The effects of climate change and extreme wildfire events on runoff erosion over a mountain watershed. *Journal of Hydrology*, *536*, 74–91. https://doi.org/10.1016/j.jhydrol.2016.02.025

Gregoretti, C., & Fontana, G. D. (2008). The triggering of debris flow due to channel-bed failure in some alpine headwater basins of the Dolomites: Analyses of critical runoff. *Hydrological Processes*, *22*(13), 2248–2263. https://doi.org/10.1002/hyp.6821

Griswold, J. P., & Iverson, R. M. (2008). *Mobility statistics and automated hazard mapping for debris flows and rock avalanches*. U.S. Geological Survey Scientific Investigations Report 2007-5276

Guilinger, J. J., Gray, A. B., Barth, N. C., & Fong, B. T. (2020). The evolution of sediment sources over a sequence of post-fire sediment-laden flows revealed through repeat high-resolution change detection. *Journal of Geophysical Research: Earth Surface*, *125*, e2020JF005527. https://doi.org/10.1029/2020JF005527

Hungerford, R. D., Harrington, M. G., Frandsen, W. H., Ryan, K. C., & Niehoff, G. J. (1991). Influence of fire on factors that affect site productivity. In *Proceedings of the symposium on management and productivity of western-Montane forest soils* (pp. 32–50).

Hungr, O., McDougall, S., & Bovis, M. (2005). Entrainment of material by debris flows. In *Debris-flow hazards and related phenomena* (pp. 135–158). Springer.

Hyde, K., Woods, S. W., & Donahue, J. (2007). Predicting gully rejuvenation after wildfire using remotely sensed burn severity data. *Geomorphology*, *86*(3), 496–511. https://doi.org/10.1016/j.geomorph.2006.10.012

Hyde, K. D., Wilcox, A. C., Jencso, K., & Woods, S. (2014). Effects of vegetation disturbance by fire on channel initiation thresholds. *Geomorphology*, *214*, 84–96. https://doi.org/10.1016/j.geomorph.2014.03.013

Iverson, R. M. (1997). The physics of debris flows. *Reviews of Geophysics*, *35*(3), 245–296. https://doi.org/10.1029/97RG00426

Iverson, R. M., Schilling, S. P., & Vallance, J. W. (1998). Objective delineation of lahar-inundation hazard zones. *The Geological Society of America Bulletin*, *110*(8), 972–984. https://doi.org/10.1130/0016-7606(1998)110<0972:odolih>2.3.co;2

Jackson, M., & Roering, J. (2009). Post-fire geomorphic response in steep, forested landscapes: Oregon Coast Range, USA. *Quaternary Science Reviews*, *28*, 1131–1146. https://doi.org/10.1016/j.quascirev.2008.05.003

James, M. R., Robson, S., & Smith, M. W. (2017). 3-d uncertainty-based topographic change detection with structure-from-motion photogrammetry: Precision maps for ground control and directly georeferenced surveys. *Earth Surface Processes and Landforms*, *42*, 1769–1788.

Jennings, Z. D., & Powers, J. M. (2015). *Official project report Los Angeles County lidar, Tech. Rep*. Oklahoma City, Oklahoma: Red Plains Surveying Company.

Jordan, P. (2016). Post-wildfire debris flows in southern British Columbia, Canada. *International Journal of Wildland Fire*, *25*(3), 322–336. https://doi.org/10.1071/WF14070

Kasprak, A., Bransky, N. D., Sankey, J. B., Caster, J., & Sankey, T. T. (2019). The effects of topographic surveying technique and data resolution on the detection and interpretation of geomorphic change. *Geomorphology*, *333*, 1–15. https://doi.org/10.1016/j.geomorph.2019.02.020

Kean, J. W., Smith, J. B., Rengers, F., McGuire, L., & Staley, D. M. (2019). Post-wildfire debris-flow monitoring data, Las Lomas, 2016 Fish Fire, Los Angeles County, California, November 2016 to February 2017. *U.S. Geological Survey Data Release*. https://doi.org/10.5066/P9F3YTBP

Kean, J. W., Staley, D. M., & Cannon, S. H. (2011). In situ measurements of post-fire debris flows in southern California: Comparisons of the timing and magnitude of 24 debris-flow events with rainfall and soil moisture conditions. *Journal of Geophysical Research: Earth Surface (2003–2012)*, *116*(F4), 116. https://doi.org/10.1029/2011JF002005

Kean, J. W., Staley, D. M., Lancaster, J. T., Rengers, F. K., Swanson, B. J., Coe, J. A., et al. (2019). Inundation, flow dynamics, and damage in the 9 January 2018 Montecito debris-flow event, California, USA: Opportunities and challenges for post-wildfire risk assessment. *Geosphere*, *15*(4), 1140–1163. https://doi.org/10.1130/GES02048.1

Kean, J. W., Staley, D. M., Leeper, R. J., Schmidt, K. M., & Gartner, J. E. (2012). A low-cost method to measure the timing of postfire flash floods and debris flows relative to rainfall. *Water Resources Research*, *48*(5), W05, 516. https://doi.org/10.1029/2011WR011460

Keeley, J. E. (1981). *Reproductive cycles and fire regimes, Tech. Rep*. WO-26. US Forest Service.

Kirchner, J. W., Finkel, R. C., Riebe, C. S., Granger, D. E., Clayton, J. L., King, J. G., & Megahan, W. F. (2001). Mountain erosion over 10 yr, 10 ky, and 10 my time scales. *Geology*, *29*(7), 591–594. https://doi.org/10.1130/0091-7613(2001)029<0591:meoyky>2.0.co;2

Laflen, J. M., Elliot, W., Flanagan, D., Meyer, C., & Nearing, M. (1997). WEPP-predicting water erosion using a process-based model. *Journal of Soil and Water Conservation*, *52*(2), 96–102.

Lague, D., Brodu, N., & Leroux, J. (2013). Accurate 3D comparison of complex topography with terrestrial laser scanner: Application to the Rangitikei canyon (NZ). *ISPRS Journal of Photogrammetry and Remote Sensing*, *82*, 10–26. https://doi.org/10.1016/j.isprsjprs.2013.04.009

Lamb, M., Scheingross, J., Amidon, W., Swanson, E., & Limaye, A. (2011). A model for fire-induced sediment yield by dry ravel in steep landscapes. *Journal of Geophysical Research*, *116*, F03006. https://doi.org/10.1029/2010JF001878

Larsen, I. J., MacDonald, L. H., Brown, E., Rough, D., Welsh, M. J., Pietraszek, J. H., et al. (2009). Causes of post-fire runoff and erosion: Water repellency, cover, or soil sealing? *Soil Science Society of America Journal*, *73*(4), 1393–1407. https://doi.org/10.2136/sssaj2007.0432

Lavé, J., & Burbank, D. (2004). Denudation processes and rates in the Transverse Ranges, southern California: Erosional response of a transitional landscape to external and anthropogenic forcing. *Journal of Geophysical Research: Earth Surface*, *109*(F1). https://doi.org/10.1029/2003JF000023

Liu, T., McGuire, L. A., Wei, H., Rengers, F. K., Gupta, H., Ji, L., & Goodrich, D. C. (2021). The timing and magnitude of changes to Hortonian overland flow at the watershed scale during the post-fire recovery process. *Hydrological Processes*, *35*(5), e14. https://doi.org/10.1002/hyp.14208

McGuire, L. A., Kean, J. W., Staley, D. M., Rengers, F. K., & Wasklewicz, T. A. (2016). Constraining the relative importance of raindrop-and flow-driven sediment transport mechanisms in postwildfire environments and implications for recovery time scales. *Journal of Geophysical Research: Earth Surface*, *121*(11), 2211–2237. https://doi.org/10.1002/2016JF003867

McGuire, L. A., Pelletier, J. D., Gómez, J. A., & Nearing, M. A. (2013). Controls on the spacing and geometry of rill networks on hillslopes: Rain splash detachment, initial hillslope roughness, and the competition between fluvial and colluvial transport. *Journal of Geophysical Research: Earth Surface*, *118*(1), 241–256. https://doi.org/10.1002/jgrf.20028

McGuire, L. A., & Rengers, F. (2019). *Las Lomas Hillside lidar*. U.S. Geological Survey Data Release. https://doi.org/10.5066/P92HVD2T

McGuire, L. A., Rengers, F. K., Kean, J. W., & Staley, D. M. (2017). Debris flow initiation by runoff in a recently burned basin: Is grain-by-grain sediment bulking or en masse failure to blame? *Geophysical Research Letters*, *44*(14), 7310–7319. https://doi.org/10.1002/2017GL074243

Meyer, G., & Wells, S. G. (1997). Fire-related sedimentation events on alluvial fans, Yellowstone National Park, USA. *Journal of Sedimentary Research*, *67*(5), 776–791. https://doi.org/10.1306/D426863A-2B26-11D7-8648000102C1865D

Meyer, G., Wells, S. G., Balling, R., Jr, & Jull, A. (1992). Response of alluvial systems to fire and climate change in Yellowstone National Park. *Nature*, *357*(6374), 147–150. https://doi.org/10.1038/357147a0

Meyer, L., Foster, G., & Nikolov, S. (1975). Effect of flow rate and canopy on rill erosion. *Transactions of the ASAE*, *18*(5), 905–0911. https://doi.org/10.13031/2013.36705

Michel, A., Kean, J., Smith, J., Allstadt, K., & Coe, J. (2019). Taking the pulse of debris flows: Extracting debris-flow dynamics from good vibrations in southern California and central Colorado. In J. Kean, J. Coe, P. Santi, & B. Guillen (Eds.), *Debris-flow hazards mitigation: Mechanics, monitoring, modeling, and assessment* (pp. 154–161). Association of Environmental and Engineering Geologists. No. 28 in Special Publication.

Minnich, R. A. (1983). Fire mosaics in southern California and northern Baja California. *Science*, *219*(4590), 1287–1294. https://doi.org/10.1126/science.219.4590.1287

Moody, J., & Ebel, B. (2012). Hyper-dry conditions provide new insights into the cause of extreme floods after wildfire. *Catena*, *93*, 58–63. https://doi.org/10.1016/j.catena.2012.01.006

Moody, J., & Martin, D. (2001). Initial hydrologic and geomorphic response following a wildfire in the Colorado Front Range. *Earth Surface Processes and Landforms*, *26*, 1049–1070. https://doi.org/10.1002/esp.253

Moody, J. A., Shakesby, R. A., Robichaud, P. R., Cannon, S. H., & Martin, D. A. (2013). Current research issues related to post-wildfire runoff and erosion processes. *Earth-Science Reviews*, *122*, 10–37. https://doi.org/10.1016/j.earscirev.2013.03.004

Moody, J. A., Smith, J. D., & Ragan, B. (2005). Critical shear stress for erosion of cohesive soils subjected to temperatures typical of wildfires. *Journal of Geophysical Research: Earth Surface*, *110*(F1). https://doi.org/10.1029/2004JF000141

Morton, D., & Miller, F. (2003). *Preliminary geologic map of the San Bernardino 30′ × 60′ quadrangle, California*. U.S. Geological Survey Open-File Report.

Moss, A. (1988). Effects of flow velocity variation on rain driven transportation and the role of rain impact in the movement of solids. *Soil Research*, *26*(3), 443–450. https://doi.org/10.1071/sr9880443

Moss, A., Walker, P., & Hutka, J. (1979). Raindrop-stimulated transportation in shallow water flows: An experimental study. *Sedimentary Geology*, *22*(3), 165–184. https://doi.org/10.1016/0037-0738(79)90051-4

Murphy, B. P., Czuba, J. A., & Belmont, P. (2019). Post-wildfire sediment cascades: A modeling framework linking debris flow generation and network-scale sediment routing. *Earth Surface Processes and Landforms*, *44*(11), 2126–2140. https://doi.org/10.1002/esp.4635

Neely, A. B., & DiBiase, R. A. (2020). Drainage area, bedrock fracture spacing, and weathering controls on landscape-scale patterns in surface sediment grain size. *Journal of Geophysical Research: Earth Surface*, *125*, e2020JF005560. https://doi.org/10.1029/2020JF005560

Nicks, A., Lane, L., & Gander, G. (1995). Weather generator. In D. Flanagan, & M. Nearing (Eds.), *USDA-Water Erosion Prediction Project: Hillslope profile and watershed model documentation, NSERL Report No. 10*. West Lafayette, IN: USDA Agricultural Research Service (ARS) National Soil Erosion Research Laboratory.

NOAA. (2005). NOAA and USGS to Conduct Pilot Project for Flash Flood and Debris Flow Warning Systems in Southern California: Improved capability will help save lives, minimize property damage and loss, News Release NOAA05-116.

NOAA. (2020). Hydrometeorological designs study center precipitation frequency data server (PFDS). http://hdsc.nws.noaa.gov/hdsc/pfds/index.html

Nobre, A. D., Cuartas, L. A., Hodnett, M., Rennó, C. D., Rodrigues, G., Silveira, A., et al. (2011). Height above the nearest drainage—A hydrologically relevant new terrain model. *Journal of Hydrology*, *404*(1–2), 13–29. https://doi.org/10.1016/j.jhydrol.2011.03.051

Noske, P. J., Nyman, P., Lane, P. N., & Sheridan, G. J. (2016). Effects of aridity in controlling the magnitude of runoff and erosion after wildfire. *Water Resources Research*, *52*(6), 4338–4357. https://doi.org/10.1002/2015WR017611

Nyman, P., Box, W. A., Stout, J. C., Sheridan, G. J., Keesstra, S. D., Lane, P. N., & Langhans, C. (2020). Debris-flow dominated sediment transport through a channel network after wildfire. *Earth Surface Processes and Landforms*, *45*, 1155–1167. https://doi.org/10.1002/esp.4785

Nyman, P., Sheridan, G. J., Moody, J. A., Smith, H. G., Noske, P. J., & Lane, P. N. (2013). Sediment availability on burned hillslopes. *Journal of Geophysical Research: Earth Surface*, *118*(4), 2451–2467. https://doi.org/10.1002/jgrf.20152

Nyman, P., Sheridan, G. J., Smith, H., & Lane, P. (2011). Evidence of debris flow occurrence after wildfire in upland catchments of southeast Australia. *Geomorphology*, *125*, 383–401. https://doi.org/10.1016/j.geomorph.2010.10.016

Nyman, P., Smith, H. G., Sherwin, C. B., Langhans, C., Lane, P. N., & Sheridan, G. J. (2015). Predicting sediment delivery from debris flows after wildfire. *Geomorphology*, *250*, 173–186. https://doi.org/10.1016/j.geomorph.2015.08.023

Oakley, N. S., Cannon, F., Munroe, R., Lancaster, J. T., Gomberg, D., & Ralph, F. M. (2018). Brief communication: Meteorological and climatological conditions associated with the 9 January 2018 post-fire debris flows in Montecito and Carpinteria, California, USA. *Natural Hazards and Earth System Sciences*, *18*(11), 3037–3043. https://doi.org/10.5194/nhess-18-3037-2018

Oakley, N. S., Lancaster, J. T., Kaplan, M. L., & Ralph, F. M. (2017). Synoptic conditions associated with cool season post-fire debris flows in the Transverse Ranges of southern California. *Natural Hazards*, *88*(1), 327–354. https://doi.org/10.1007/s11069-017-2867-6

Orem, C. A., & Pelletier, J. D. (2015). Quantifying the time scale of elevated geomorphic response following wildfires using multi-temporal LiDAR data: An example from the Las Conchas fire, Jemez Mountains, New Mexico. *Geomorphology*, *232*, 224–238. https://doi.org/10.1016/j.geomorph.2015.01.006

Palucis, M. C., Ulizio, T. P., & Lamb, M. P. (2021). Debris flow initiation from ravel-filled channel bed failure following wildfire in a bedrock landscape with limited sediment supply. *GSA Bulletin*. https://doi.org/10.1130/B35822.1

Parise, M., & Cannon, S. (2012). Wildfire impacts on the processes that generate debris flows in burned watersheds. *Natural Hazards*, *61*(1), 217–227. https://doi.org/10.1007/s11069-011-9769-9

Parsons, A., Robichaud, P., Lewis, S., Napper, C., Clark, J., & Jain, T. (2010). *Field guide for mapping post-fire soil burn severity. Tech. rep*. General Technical Report RMRS-GTR-243. Fort Collins, CO: USDA Forest Service, Rocky Mountain Research Station.

Pelletier, J. D., & Orem, C. A. (2014). How do sediment yields from post-wildfire debris-laden flows depend on terrain slope, soil burn severity class, and drainage basin area? Insights from airborne-LiDAR change detection. *Earth Surface Processes and Landforms*, *39*(13), 1822–1832. https://doi.org/10.1002/esp.3570

Pierce, J., & Meyer, G. (2008). Long-term fire history from alluvial fan sediments: The role of drought and climate variability, and implications for management of rocky mountain forests. *International Journal of Wildland Fire*, *17*(1), 84–95. https://doi.org/10.1071/WF07027

Pietraszek, J. H. (2006). *Controls on post-fire erosion at the hillslope scale, Colorado Front Range (Ph.D. thesis)*. Fort Collins, CO: Colorado State University.

PRISM Climate Group Oregon State University. (2004). *PRISM climate data*. http://prism.oregonstate.edu

Prochaska, A. B., Santi, P. M., & Higgins, J. D. (2008). Debris basin and deflection berm design for fire-related debris-flow mitigation. *Environmental and Engineering Geoscience*, *14*(4), 297–313. https://doi.org/10.2113/gseegeosci.14.4.297

Prochaska, A. B., Santi, P. M., Higgins, J. D., & Cannon, S. H. (2008). Debris-flow runout predictions based on the average channel slope (ACS). *Engineering Geology*, *98*(1–2), 29–40. https://doi.org/10.1016/j.enggeo.2008.01.011

Reneau, S. L., Katzman, D., Kuyumjian, G. A., Lavine, A., & Malmon, D. V. (2007). Sediment delivery after a wildfire. *Geology*, *35*(2), 151–154. https://doi.org/10.1130/G23288A.1

Rengers, F., Lunacek, M., & Tucker, G. (2016). Application of an evolutionary algorithm for parameter optimization in a gully erosion model. *Environmental Modelling & Software*, *80*, 297–305. https://doi.org/10.1016/j.envsoft.2016.02.033

Rengers, F., & McGuire, L. (2018). Quantifying post-wildfire hillslope erosion with lidar. In *The Fifth International Conference on Geomorphometry, Boulder, CO* (pp. 1–4).

Rengers, F., McGuire, L., Kean, J., Staley, D., & Youberg, A. (2019). Progress in simplifying hydrologic model parameterization for broad applications to post-wildfire flooding and debris-flow hazards. *Earth Surface Processes and Landforms*, *44*(15), 3078–3092. https://doi.org/10.1002/esp.4697

Rengers, F., & Tucker, G. (2014). Analysis and modeling of gully headcut dynamics, North American high plains. *Journal of Geophysical Research: Earth Surface*, *119*, 983–1003. https://doi.org/10.1002/2013JF002962

Rengers, F., & Tucker, G. (2015). The evolution of gully headcut morphology: A case study using terrestrial laser scanning and hydrological monitoring. *Earth Surface Processes and Landforms*, *40*, 1304–1317. https://doi.org/10.1002/esp.3721

Rengers, F., Tucker, G. E., Moody, J. A., & Ebel, B. A. (2016). Illuminating wildfire erosion and deposition patterns with repeat terrestrial lidar. *Journal of Geophysical Research: Earth Surface*, *121*, 588–608. https://doi.org/10.1002/2015JF003600

Rengers, F. K., McGuire, L., Ebel, B. A., & Tucker, G. (2018). The evolution of a colluvial hollow to a fluvial channel with periodic steps following two transformational disturbances: A wildfire and a historic flood. *Geomorphology*, *309*, 121–130. https://doi.org/10.1016/j.geomorph.2018.01.003

Rengers, F. K., McGuire, L. A., Oakley, N. S., Kean, J. W., Staley, D. M., & Tang, H. (2020). Landslides after wildfire: Initiation, magnitude, and mobility. *Landslides*, *17*(11), 2631–2641. https://doi.org/10.1007/s10346-020-01506-3

Rengers, F. K., Pagonis, V., & Mahan, S. A. (2017). Can thermoluminescence be used to determine soil heating from a wildfire? *Radiation Measurements*, *107*, 119–127. https://doi.org/10.1016/j.radmeas.2017.09.002

Rengers, F. K., Tucker, G., & Mahan, S. (2016). Episodic bedrock erosion by gully-head migration, Colorado High Plains, USA. *Earth Surface Processes and Landforms*, *41*(11), 1574–1582. https://doi.org/10.1002/esp.3929

Robichaud, P., Elliot, W., Pierson, F., Hall, D., & Moffet, C. (2007). Predicting postfire erosion and mitigation effectiveness with a web-based probabilistic erosion model. *Catena*, *71*(2), 229–241. https://doi.org/10.1016/j.catena.2007.03.003

Robichaud, P., Wagenbrenner, J., Brown, R., Wohlgemuth, P., & Beyers, J. (2008). Evaluating the effectiveness of contour-felled log erosion barriers as a post-fire runoff and erosion mitigation treatment in the western United States. *International Journal of Wildland Fire*, *17*(2), 255–273. https://doi.org/10.1071/WF07032

Robichaud, P., Wagenbrenner, J. W., Pierson, F. B., Spaeth, K. E., Ashmun, L. E., & Moffet, C. A. (2016). Infiltration and interrill erosion rates after a wildfire in western Montana, USA. *Catena*, *142*, 77–88. https://doi.org/10.1016/j.catena.2016.01.027

Robichaud, P. R. (2005). Measurement of post-fire hillslope erosion to evaluate and model rehabilitation treatment effectiveness and recovery. *International Journal of Wildland Fire*, *14*(4), 475–485. https://doi.org/10.1071/WF05031

Robichaud, P. R., Dobre, M., Lew, R., Brooks, E. S., Miller, M. E., & Elliot, W. (2019). Beyond the horizon: WEPPcloud-PEP, Postfire Erosion Prediction Tool. In American Geophysical Union, Fall Meeting 2019, H31H-05, San Francisco, California.

Robichaud, P. R., Rhee, H., & Lewis, S. A. (2014). A synthesis of post-fire Burned Area Reports from 1972 to 2009 for western US Forest Service lands: Trends in wildfire characteristics and post-fire stabilization treatments and expenditures. *International Journal of Wildland Fire*, *23*(7), 929–944. https://doi.org/10.1071/WF13192

Robinne, F.-N., Miller, C., Parisien, M.-A., Emelko, M. B., Bladon, K. D., Silins, U., & Flannigan, M. (2016). A global index for mapping the exposure of water resources to wildfire. *Forests*, *7*(1), 22. https://doi.org/10.3390/f7010022

Santi, P. M., Higgins, J. D., Cannon, S. H., Gartner, J. E., & Gartner, J. E. (2008). Sources of debris flow material in burned areas. *Geomorphology*, *96*(3), 310–321. https://doi.org/10.1016/j.geomorph.2007.02.022

Santi, P. M., & Rengers, F. K. (2020). *Wildfire and Landscape Change, in Reference module in earth systems and environmental sciences*. Elsevier. https://doi.org/10.1016/B978-0-12-818234-5.00017-1

Schilling, S. P. (1998). *LAHARZ; GIS programs for automated mapping of lahar-inundation hazard zones*. Information Services 98-638. U.S. Geological Survey.

Shakesby, R., & Doerr, S. (2006). Wildfire as a hydrological and geomorphological agent. *Earth-Science Reviews*, *74*(3), 269–307. https://doi.org/10.1016/j.earscirev.2005.10.006

Srivastava, A., Flanagan, D., Frankenberger, J., & Engel, B. (2019). Updated climate database and impacts on WEPP model predictions. *Journal of Soil and Water Conservation*, *74*(4), 334–349. https://doi.org/10.2489/jswc.74.4.334

Staley, D. M., Wasklewicz, T. A., & Kean, J. W. (2014). Characterizing the primary material sources and dominant erosional processes for post-fire debris-flow initiation in a headwater basin using multi-temporal terrestrial laser scanning data. *Geomorphology*, *214*, 324–338. https://doi.org/10.1016/j.geomorph.2014.02.015

Surian, N., Righini, M., Lucía, A., Nardi, L., Amponsah, W., Benvenuti, M., et al. (2016). Channel response to extreme floods: Insights on controlling factors from six mountain rivers in northern Apennines, Italy. *Geomorphology*, *272*, 78–91. https://doi.org/10.1016/j.geomorph.2016.02.002

Takahashi, T. (1978). Mechanical characteristics of debris flow. *Journal of the Hydraulics Division*, *104*(8), 1153–1169. https://doi.org/10.1061/jyceaj.0005046

Tang, H., McGuire, L. A., Rengers, F. K., Kean, J. W., Staley, D. M., & Smith, J. B. (2019). Evolution of debris flow initiation mechanisms and sediment sources during a sequence of post-wildfire rainstorms. *Journal of Geophysical Research*, *124*, 1572–1595. https://doi.org/10.1029/2018JF004837

Tarboton, D. G., Bras, R. L., & Rodriguez-Iturbe, I. (1991). On the extraction of channel networks from digital elevation data. *Hydrological Processes*, *5*(1), 81–100. https://doi.org/10.1002/hyp.3360050107

Thompson, C., & Croke, J. (2013). Geomorphic effects, flood power, and channel competence of a catastrophic flood in confined and unconfined reaches of the upper Lockyer valley, southeast Queensland, Australia. *Geomorphology*, *197*, 156–169. https://doi.org/10.1016/j.geomorph.2013.05.006

Tillery, A. C., & Rengers, F. K. (2020). Controls on debris-flow initiation on burned and unburned hillslopes during an exceptional rainstorm in southern New Mexico, USA. *Earth Surface Processes and Landforms*, *45*(4), 1051–1066. https://doi.org/10.1002/esp.4761

Tucker, G. E., & Bras, R. L. (2000). A stochastic approach to modeling the role of rainfall variability in drainage basin evolution. *Water Resources Research*, *36*(7), 1953–1964. https://doi.org/10.1029/2000wr900065

Tucker, G. E., Lancaster, S. T., Gasparini, N. M., & Bras, R. L. (2001). The channel-hillslope integrated landscape development (CHILD) model. In R. S. Harmon, & W. W. I. Doe (Eds.), *Landscape erosion and evolution modeling* (pp. 349–388). New York: Springer. https://doi.org/10.1007/978-1-4615-0575-4_12

Ulery, A., Graham, R., & Bowen, L. (1996). Forest fire effects on soil phyllosilicates in California. *Soil Science Society of America Journal*, *60*(1), 309–315. https://doi.org/10.2136/sssaj1996.03615995006000010047x

U.S. Department of Agriculture. (2020). *Web soil survey, natural resources conservation service*. https://websoilsurvey.sc.egov.usda.gov/App/WebSoilSurvey.aspx

Valente, F., David, J., & Gash, J. (1997). Modeling interception loss for two sparse eucalypt and pine forests in central portugal using reformulated rutter and gash analytical models. *Journal of Hydrology*, *190*(1), 141–162. https://doi.org/10.1016/s0022-1694(96)03066-1

Wagenbrenner, J. W., & Robichaud, P. R. (2014). Post-fire bedload sediment delivery across spatial scales in the interior western United States. *Earth Surface Processes and Landforms*, *39*(7), 865–876. https://doi.org/10.1002/esp.3488

Wester, T., Wasklewicz, T., & Staley, D. (2014). Functional and structural connectivity within a recently burned drainage basin. *Geomorphology*, *206*, 362–373. https://doi.org/10.1016/j.geomorph.2013.10.011

Wohl, E. (2010). A brief review of the process domain concept and its application to quantifying sediment dynamics in bedrock canyons. *Terra Nova*, *22*(6), 411–416. https://doi.org/10.1111/j.1365-3121.2010.00950.x

Wohl, E., & Scott, D. N. (2017). Transience of channel head locations following disturbance. *Earth Surface Processes and Landforms*, *42*(7), 1132–1139. https://doi.org/10.1002/esp.4124

Wohl, E. E. (2013). Migration of channel heads following wildfire in the Colorado Front Range, USA. *Earth Surface Processes and Landforms*, *38*(9), 1049–1053. https://doi.org/10.1002/esp.3429

Yochum, S. E., Sholtes, J. S., Scott, J. A., & Bledsoe, B. P. (2017). Stream power framework for predicting geomorphic change: The 2013 Colorado Front Range flood. *Geomorphology*, *292*, 178–192. https://doi.org/10.1016/j.geomorph.2017.03.004

Zedler, P. H. (1995). Fire frequency in southern California shrublands: Biological effects and management options. In J. E. Keeley, & T. Scott (Eds.), *Brushfires in California wildlands: Ecology and resource management* (pp. 101–112). Fairfield, WA: International Association of Wildland Fire.